

# Towards 21-cm Intensity Mapping at $z = 2.28$ with uGMRT using the Tapered Gridded Estimator I: Foreground Avoidance

Srijita Pal,<sup>1\*</sup> Kh. Md. Asif Elahi,<sup>1</sup> Somnath Bharadwaj,<sup>1†</sup> Sk. Saiyad Ali,<sup>2</sup> Samir Choudhuri,<sup>3,4</sup> Abhik Ghosh,<sup>5</sup> Arnab Chakraborty,<sup>6</sup> Abhirup Datta,<sup>7</sup> Nirupam Roy,<sup>8</sup> Madhurima Choudhury,<sup>9,7</sup> Prasun Dutta<sup>10</sup>

<sup>1</sup> Department of Physics and Centre for Theoretical Studies, IIT Kharagpur, Kharagpur 721 302, India

<sup>2</sup> Department of Physics, Jadavpur University, Kolkata 700032, India

<sup>3</sup> Astronomy Unit, Queen Mary University of London, Mile End Road, London E1 4NS, United Kingdom

<sup>4</sup> Centre for Strings, Gravitation and Cosmology, Department of Physics, Indian Institute of Technology Madras, Chennai 600036, India

<sup>5</sup> Department of Physics, Banwarilal Bhalotia College, Asansol, West Bengal-713303, India

<sup>6</sup> Department of Physics and McGill Space Institute, McGill University, Montreal, QC, Canada H3A 2T8

<sup>7</sup> Discipline of Astronomy, Astrophysics and Space Engineering, Indian Institute of Technology Indore, Indore 453552, India

<sup>8</sup> Department of Physics, Indian Institute of Science, Bangalore 560012, India

<sup>9</sup> ARCO (Astrophysics Research Center), Department of Natural Sciences, The Open University of Israel, 1 University Road, PO Box 808, Ra'anana 4353701, Israel

<sup>10</sup> Department of Physics, IIT (BHU), Varanasi, 221005 India

Accepted XXX. Received YYY; in original form ZZZ

## ABSTRACT

The post-reionization ( $z \leq 6$ ) neutral hydrogen (H I) 21-cm intensity mapping signal holds the potential to probe the large scale structures, study the expansion history and constrain various cosmological parameters. Here we apply the Tapered Gridded Estimator (TGE) to estimate  $P(k_{\perp}, k_{\parallel})$  the power spectrum of the  $z = 2.28$  (432.8 MHz) redshifted 21-cm signal using a 24.4 MHz sub-band drawn from uGMRT Band 3 observations of European Large-Area ISO Survey-North 1 (ELAIS-N1). The TGE allows us to taper the sky response which suppresses the foreground contribution from sources in the periphery of the telescope's field of view. We apply the TGE on the measured visibility data to estimate the multi-frequency angular power spectrum (MAPS)  $C_{\ell}(\Delta\nu)$  from which we determine  $P(k_{\perp}, k_{\parallel})$  using maximum-likelihood which naturally overcomes the issue of missing frequency channels (55 % here). The entire methodology is validated using simulations. For the data, using the foreground avoidance technique, we obtain a  $2\sigma$  upper limit of  $\Delta^2(k) \leq (133.97)^2 \text{ mK}^2$  for the 21-cm brightness temperature fluctuation at  $k = 0.347 \text{ Mpc}^{-1}$ . This corresponds to  $[\Omega_{\text{H I}} b_{\text{H I}}] \leq 0.23$ , where  $\Omega_{\text{H I}}$  and  $b_{\text{H I}}$  respectively denote the cosmic H I mass density and the H I bias parameter. A previous work has analyzed 8 MHz of the same data at  $z = 2.19$ , and reported  $\Delta^2(k) \leq (61.49)^2 \text{ mK}^2$  and  $[\Omega_{\text{H I}} b_{\text{H I}}] \leq 0.11$  at  $k = 1 \text{ Mpc}^{-1}$ . The upper limits presented here are still orders of magnitude larger than the expected signal corresponding to  $\Omega_{\text{H I}} \sim 10^{-3}$  and  $b_{\text{H I}} \sim 2$ .

**Key words:** methods: statistical, data analysis - techniques: interferometric cosmology: diffuse radiation, large-scale structure of Universe

## 1 INTRODUCTION

Intensity mapping with the neutral hydrogen (H I) 21-cm line is a progressing tool to probe the large scale structures of the post-reionization Universe (Bharadwaj et al. 2001; Bharadwaj & Sethi 2001). It can independently assess the expansion history of the Universe by measuring the Baryon Acoustic Oscillation (BAO) in the 21-cm power spectrum (PS) (Wyithe et al. 2008; Chang et al. 2008; Seo et al. 2010). It is also possible to constrain various cosmological parameters using measurements of the 21-cm PS without reference to the BAO (Bharadwaj et al. 2009; Visbal et al. 2009). Further it is possible to quantify higher order statistics, such as bispectrum,

to study non-Gaussianity (Bharadwaj & Ali 2005; Hazra & Guha Sarkar 2012).

There has been several successful 21-cm intensity mapping experiments (Pen et al. 2009; Chang et al. 2010; Masui et al. 2013; Switzer et al. 2013; Anderson et al. 2018; Wolz et al. 2021) at low-redshifts ( $z < 1$ ). Most of these experiments have used single dish telescopes, and they have detected the 21-cm signal by cross-correlating their measurements with existing galaxy redshift surveys. Switzer et al. (2013) have detected the 21-cm intensity mapping signal in auto-correlation at  $z = 0.8$  using the Green Bank Telescope. Recently, CHIME<sup>1</sup> (CHIME Collaboration et al. 2022) has made the first interferometric 21-cm intensity mapping measurements in the redshift range  $0.78 < z < 1.43$  using cross-correlations with

\* E-mail: srijitapal.phy@gmail.com

† E-mail: somnath@phy.iitkgp.ac.in

<sup>1</sup> <https://chime-experiment.ca/en/>

luminous red galaxies, emission line galaxies, and quasars. Several other radio interferometers such as BINGO<sup>2</sup> (Wuensche 2019), the Tianlai project<sup>3</sup> (Chen 2012), HIRAX<sup>4</sup> (Newburgh et al. 2016) and MeerKAT<sup>5</sup> (Kennedy & Bull 2021) particularly focus on measuring the BAO to study the nature of Dark Energy. The Ooty Radio Telescope (ORT; Swarup et al. 1971) is being upgraded to the Ooty Wide Field Array (OWFA<sup>6</sup>; Subrahmanya et al. 2017) to measure the 21-cm PS at  $z \sim 3.35$ . Furthermore, the next-generation intensity mapping surveys, with the Square Kilometer Array (SKA<sup>7</sup>; Bull et al. 2015) hold the potential to provide a large cosmological window to the post-reionization era.

The Giant Metrewave Radio Telescope (GMRT<sup>8</sup>; Swarup et al. 1991) is sensitive to the post-reionization 21-cm intensity mapping signal from a broad redshift range ( $z \leq 6$ ; Bharadwaj & Pandey 2003; Bharadwaj & Srikant 2004). In an effort towards this Ghosh et al. (2011a,b) have analyzed 610 MHz GMRT data to place an upper limit  $[\bar{x}_{\text{H I}} b_{\text{H I}}] < 2.9$  where  $\bar{x}_{\text{H I}}$  and  $b_{\text{H I}}$  are the mean neutral fraction and bias parameter respectively at redshift  $z = 1.32$ . We note that this corresponds to  $[\Omega_{\text{H I}} b_{\text{H I}}] < 0.11$  where  $\Omega_{\text{H I}}$  is the comoving H I mass density in units of the present critical density. In a recent work Chakraborty et al. (2021) (hereafter Ch21) have analyzed several 8 MHz subsets drawn from 200 MHz upgraded GMRT (uGMRT; Gupta et al. 2017) data to estimate the 21-cm PS at multiple redshifts in the range  $1.96 < z < 3.58$  and place the upper limits  $[\Omega_{\text{H I}} b_{\text{H I}}] < 0.09, 0.11, 0.12$ , and  $0.24$  at  $z = 1.96, 2.19, 2.62$  and  $3.58$  respectively.

The Tapered Gridded Estimator (TGE; Choudhuri et al. 2014, 2016a) is a visibility based PS estimator which allows us to taper the sky response to suppress the contribution from bright sources located in the side-lobes and the periphery of the telescope's field of view. Further, the TGE works with the gridded visibilities which makes it computationally fast. The TGE also uses the measured visibility data to internally evaluate the noise bias and subtracts this to provide an unbiased estimate of the PS. Bharadwaj et al. (2018) (hereafter, Paper I) have proposed the TGE to estimate  $C_\ell(\Delta\nu)$  the multi-frequency angular power spectrum (MAPS; Datta et al. 2007; Mondal et al. 2019) which characterizes the second order statistics of the sky signal jointly as a function of the angular multipole  $\ell$  and frequency separation  $\Delta\nu$ . They use  $C_\ell(\Delta\nu)$  to determine the cylindrical power spectrum of the 21-cm brightness temperature fluctuations  $P(k_\perp, k_\parallel)$  which is related to  $C_\ell(\Delta\nu)$  through a Fourier transform with respect to  $\Delta\nu$ . Using simulated visibility data, they show that this estimator can accurately recover the input model PS even when 80% randomly chosen frequency channels are flagged. A salient feature of this estimator is that it only uses the available data, and it is not necessary to make any assumption regarding the data values in the missing frequency channels. In a recent paper Pal et al. (2021) (hereafter Paper II) have demonstrated the capabilities of the TGE by using the TGE to estimate  $P(k_\perp, k_\parallel)$  from a 150 MHz GMRT observational data where 47% of the frequency channels are flagged due to Radio Frequency Interference (RFI). They obtain a  $2\sigma$  upper limit of  $(72.66)^2 \text{ K}^2$  on the mean squared H I 21-cm brightness temperature fluctuations at  $k = 1.59 \text{ Mpc}^{-1}$ . We note that the two dimensional (2D) TGE for the angular power spectrum  $C_\ell$  has been extensively

**Table 1.** Observation summary

Working antennas	28
Central Frequency	400 MHz
Number of Channels	8192
Channel width	24.4 kHz
Bandwidth	200 MHz
Total observation time	25 h
Integration time	2 s
Target field ( $\alpha, \delta$ ) <sub>2000</sub>	( $16^{\text{h}} 10^{\text{m}} 1^{\text{s}}$ , $+54^\circ 30' 36''$ )
Galactic coordinates ( $l, b$ )	$86.95^\circ, +44.48^\circ$

used to study the foregrounds for cosmological 21-cm observations (Choudhuri et al. 2017, 2020; Chakraborty et al. 2019a; Mazumder et al. 2020) and also magnetohydrodynamics turbulence in supernova remnants (Saha et al. 2019; Saha et al. 2021).

In this work we consider uGMRT Band 3 (300 – 500 MHz) data of the ELAIS N1 field. Chakraborty et al. (2019b) have analysed this data and used the 2D TGE to study the angular and spectral variation of  $C_\ell(\nu)$  for the diffuse galactic synchrotron emission. As mentioned earlier, Ch21 have analysed this data using a delay spectrum approach to estimate the PS of the 21-cm intensity mapping signal. The difficulty arises because the missing frequency channels (flagged due to RFI) introduce artefacts in delay space which corrupt the estimated PS. Ch21 have overcome this by using one dimensional complex CLEAN (Parsons & Backer 2009) to compensate for the missing frequency channels. Considering the same data, the present work uses a bandwidth of 24.4 MHz centred at 432.8 MHz. Here we have applied the TGE to estimate the MAPS and PS  $P(k_\perp, k_\parallel)$ . We study the capabilities of this estimator to (1) suppress the wide-field foregrounds, and (2) deal with the missing frequency channels. We also present results for the spherically binned power spectrum, and present an upper limit for  $[\Omega_{\text{H I}} b_{\text{H I}}]$  at  $z = 2.28$ .

The paper is arranged as follows. Section 2 summarizes the observations and the preliminary processing of the data which has been used here. Section 3 presents the methodology how TGE is used to estimate  $C_\ell(\Delta\nu)$  and  $P(k_\perp, k_\parallel)$  from the observed visibility data, and in Section 4 we have validated the methodology using simulations. Our results are presented in Section 5, and we present a summary and conclusion in Section 6.

Throughout this paper, unless mentioned otherwise, we have used a  $\Lambda$ CDM cosmology with the parameters  $\Omega_m = 0.309$ ,  $h = 0.67$ ,  $n_s = 0.965$ , and  $\Omega_b h^2 = 0.0224$  which are in reasonable agreement with the present observations (Planck Collaboration et al. 2020).

## 2 OBSERVATIONS AND DATA ANALYSIS

The observations were carried out using the GMRT array configuration (Swarup et al. 1991). The recently upgraded version of GMRT (uGMRT) provides a frequency coverage of 120 – 1500 MHz with 400 MHz maximum instantaneous available bandwidth and an improved receiver system with higher  $G/T_{\text{sys}}$  for high dynamic range imaging (Gupta et al. 2017). We have observed the field European Large-Area ISO Survey-North 1 (ELAIS-N1;  $\alpha_{2000} = 16^{\text{h}} 10^{\text{m}} 1^{\text{s}}$ ,  $\delta_{2000} = 54^\circ 30' 36''$ ) with the uGMRT at Band

<sup>2</sup> <https://bingotelescope.org/>

<sup>3</sup> <http://tianlai.bao.ac.cn/>

<sup>4</sup> <https://hirax.ukzn.ac.za/>

<sup>5</sup> <https://www.sarao.ac.za/science/meerkat/>

<sup>6</sup> <http://rac.ncra.tifr.res.in/ort.html>

<sup>7</sup> <https://www.skatelescope.org/>

<sup>8</sup> <http://www.gmrt.ncra.tifr.res.in/>

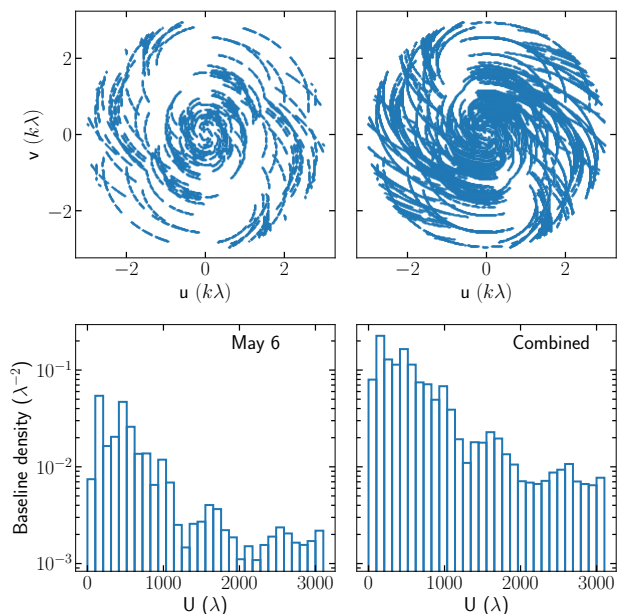


**Figure 1.** The upper panels show the uv-coverage for the May 6 data (left panel) and the combined nights data (right panel) considering baselines of length  $U \leq 3000\lambda$  at  $\nu_c = 432.8$  MHz. The corresponding baseline density (number of baselines per unit area of the uv plane) is shown as a function of  $U$  in the lower panels.

3 (300 – 500 MHz) during May 2017 for 25 hours over four days. The primary calibrators 3C286 and 3C48 have been used to scale the overall flux of the observation. We have also used a nearby phase calibrator (J1549+506) to correct the antenna gains’ temporal variation. The total bandwidth of the observation is 200 MHz with a frequency resolution of 24.4 kHz. We have taken the data with a high time resolution (2 s) to identify and remove the RFI. The observations were carried out mainly at night to minimize the RFI. The relevant observational parameters have been summarized in Table 1.

The details of the initial data analysis are given in Chakraborty et al. (2019a,b). Here, we briefly summarize the flagging and calibration steps adopted. For initial RFI flagging, we use the `AOFLAGGER` which detects any anomaly in time-frequency domain per baseline per polarization and discards the corrupt data (Offringa et al. 2010; Offringa, A. R. et al. 2012). We discard 5% of the total number of channels (2.5% on each side) due to a bad bandspace at the edge of the bandwidth. We take the direction-independent approach to calibrate the data using the Common Astronomy Software Applications (CASA; McMullin et al. 2007). We start with an initial gain and bandpass calibration of the primary calibrators and remove residual RFIs from the calibrated data using the `RFLAG` routine of CASA. After doing this twice, we perform a final bandpass and delay calibration on the primary calibrators. We next rectify the temporal variation of the amplitude and the phase of the antenna gains using the secondary calibrator. Finally, we apply the gain solutions to the target field and split this out for imaging. The final off-source r.m.s. noise is  $\sim 15\mu\text{Jy beam}^{-1}$  which is nearly 3.5 times higher than the theoretically expected noise. Note that we have calculated the theoretical noise using the specifications of uGMRT for Band 3 (Gupta et al. 2017), and considering the parameters of our observations. The excess noise in the image can thus be caused due to a difference in the system temperature depending on the direction of sky we have ob-

**Table 2.** Considering the sub-band 2 with central frequency  $\nu_c = 432.8$  MHz, spectral resolution  $\Delta\nu_c = 24.4$  kHz and bandwidth  $B_{bw} = 24.4$  MHz, we tabulate the flagging fraction and r.m.s. of the visibilities  $\sigma_N$  for different nights of observation

Night of observation	flag (%)	r.m.s. $\sigma_N$ (Jy)
May 5	70.97	0.431337
May 6	13.07	0.394103
May 7	42.75	0.473156
May 27	71.29	0.445912
All nights combined	54.81	0.430112

served; this may also be caused due to residual deconvolution errors during imaging, residual calibration errors etc. Hence, we expect this excess noise to further contribute as excess power in the estimated power spectrum as residual foregrounds and systematics, as well as increase the error budget (the r.m.s. fluctuations) of the power spectrum estimated from the data (Kumar et al. 2020, 2022). Post four rounds of self-calibration (only phase), we have identified and subtracted out the compact and discrete sources with flux densities  $> 100\mu\text{Jy}$  within an area of  $1.8\text{ deg}^2$  using the task `UVSUB` in CASA. The residual visibility data is used for the subsequent analysis presented here.

The baseline distribution and various telescope parameters change with frequency across the 200 MHz uGMRT bandwidth. For the subsequent analysis we have divided the total bandwidth into eight sub-bands (namely, sub-bands 0 to 7). The bandwidth of each sub-band  $\sim 24.4$  MHz is less than 10% of the central frequency of the corresponding sub-band, which allows us to ignore the baseline migration and change in telescope parameters within the sub-band. This is a fair assumption considering Section 4 where we validate our estimator for the data considered here. We have checked the quality of the data in each of the sub-bands in terms of the percentage of flagged channels and the variance of the data. The May 6 observation from the sub-band 2 is found to have the least percentage of flagging and the smallest visibility r.m.s. Guided by this, we have entirely restricted the subsequent analysis of this paper to sub-band 2 which is centred at  $\nu_c = 432.8$  MHz and contains 1000 channels with spectral resolution  $\Delta\nu_c = 24.4$  kHz. In addition to the individual nights data, we have also combined the four nights data using the `CONCAT` task of CASA. The flagging statistics and r.m.s. values of the individual nights and the combined nights data are given in Table 2.

The upper panels of Figure 1 show the baseline distributions for the May 6 data (left panel) and the combined nights data (right panel) for a single channel at the central frequency. The lower panels show the baseline density, *i.e.*, the number of baselines per unit area of the uv-plane, as a function of baseline length  $U = |U|$ .

### 3 METHODOLOGY

The multi-frequency angular power spectrum (MAPS)  $C_\ell(\nu_a, \nu_b)$  jointly characterizes the statistical properties of the sky signal as a function of the angular multipoles and frequency. The brightness temperature fluctuations in the sky is decomposed in terms of the spherical harmonics  $Y_\ell^m(\hat{n})$  as,

$$\delta T_b(\hat{n}, \nu) = \sum_{\ell, m} a_{\ell m}(\nu) Y_\ell^m(\hat{n}), \quad (1)$$

and the MAPS is defined as

$$C_\ell(v_a, v_b) = \langle a_{\ell m}(v_a) a_{\ell m}^*(v_b) \rangle \quad (2)$$

where  $\langle \dots \rangle$  denotes an ensemble average over different statistically independent realizations of the random field  $\delta T_b(\hat{n}, \nu)$ .

The details of the visibility based TGE for measuring the MAPS and the PS are given in [Paper I](#) and [Paper II](#). Here, we briefly summarize the mathematical formalism for this estimator. Starting from the visibility data,  $\mathcal{V}_i(v_a)$  corresponding to the  $i$ -th baseline  $\mathbf{U}_i$  and frequency  $v_a$ , the TGE first convolves the measured  $\mathcal{V}_i(v_a)$  with  $\tilde{w}(\mathbf{U})$  which is the Fourier transform of a window function  $\mathcal{W}(\theta)$  suitably chosen to taper the primary beam (PB) of the telescope far away from the phase center. We divide the  $uv$  plane in a rectangular grid and the convolved visibilities  $\mathcal{V}_{cg}$  at the grid-point  $\mathbf{U}_g$  is given by,

$$\mathcal{V}_{cg}(v_a) = \sum_i \tilde{w}(\mathbf{U}_g - \mathbf{U}_i) \mathcal{V}_i(v_a) F_i(v_a). \quad (3)$$

Here the subscript ‘ $a$ ’ denotes an individual channel and  $a = 1, 2, \dots, N_c$  where  $N_c$  is the total number of channels that cover a bandwidth  $B_{bw}$ . The factor  $F_i(v_a)$  is used to incorporate the flagging information.  $F_i(v_a)$  is assigned a value ‘0’ if the data at the baseline  $\mathbf{U}_i$  and frequency  $v_a$  is flagged and  $F_i(v_a)$  is ‘1’ otherwise.

We use a Gaussian window function,  $\mathcal{W}(\theta) = e^{-\theta^2/\theta_w^2}$ , to taper the sky signal away from the phase center. The main lobe of the PB of any telescope with a circular aperture can be approximated as,  $\mathcal{A}(\theta) = e^{-\theta^2/\theta_0^2}$  where  $\theta_0 \sim 0.6 \times \theta_{\text{FWHM}}$ ,  $\theta_{\text{FWHM}}$  being the full width at half maxima of  $\mathcal{A}(\theta)$  ([Bharadwaj & Sethi 2001](#); [Choudhuri et al. 2014](#)). We choose  $\theta_w = f\theta_0$ , where ‘ $f$ ’ represents the tapering parameter and controls the degree to which the PB pattern is tapered. The convolution implemented in eq. (3) equivalently amounts to modulating  $\mathcal{A}(\theta)$  with  $\mathcal{W}(\theta)$  by a multiplication, where  $f > 1$  will provide very little tapering and  $f < 1$  can be used to highly suppress the PB away from the phase center.

We define the TGE for MAPS in [Paper I](#) as,

$$\hat{E}_g(v_a, v_b) = M_g^{-1}(v_a, v_b) \mathcal{R}e \left[ \mathcal{V}_{cg}(v_a) \mathcal{V}_{cg}^*(v_b) - \delta_{a,b} \sum_i F_i(v_a) |\tilde{w}(\mathbf{U}_g - \mathbf{U}_i)|^2 |\mathcal{V}_i(v_a)|^2 \right] \quad (4)$$

where  $\mathcal{R}e[\dots]$  refers to real part of the expression within the brackets [...] and  $M_g(v_a, v_b)$  is a normalization constant (discussed in detail later in this section). Along with the sky signal, each visibility  $\mathcal{V}_i(v_a)$  contains an additive noise component  $\mathcal{N}_i(v_a)$  that is assumed to be a Gaussian random variable with zero mean and variance  $2\sigma_N^2$ . The noise in different baselines, frequency channels and timestamps are uncorrelated. Consequently, the noise contribution in MAPS is restricted only to the self-correlations of the visibilities

$$\langle \mathcal{N}_i(v_a) \mathcal{N}_j^*(v_b) \rangle = \delta_{i,j} \delta_{a,b} 2\sigma_N^2. \quad (5)$$

The second term in the square brackets [...] in eq. (4) subtracts out the contribution from the self correlation of a visibility *i.e.* same baseline, frequency channel and timestamp. This exactly cancels out the noise contribution in the first term, and we obtain an unbiased estimate of MAPS.

We have validated eq. (4) (hereafter referred to as TGE-I) in [Paper I](#) using realistic 150 MHz GMRT simulations. We have shown there that in the absence of foregrounds TGE-I can recover an input model 21-cm PS with a very high accuracy even in the presence of noise and 80% flagging in the visibility data. However, the data available from the past and current 21-cm experiments are dominated by various

foregrounds that overshadow the noise and the 21-cm signal by a few orders of magnitude ([Ghosh et al. 2011a,b](#)). We find (shown later) that  $C_\ell(v_a, v_b)$  estimated by applying TGE-I to such foreground dominated data shows a discontinuity at  $v_a = v_b$ . This discontinuity arises due to the self-correlation term which is subtracted out only for  $v_a = v_b$  in TGE-I. We also find that this discontinuity introduces a negative bias in the estimated PS  $P(k)$ . To deal with this problem, we have slightly modified TGE-I in [Paper II](#) to obtain

$$\hat{E}_g(v_a, v_b) = M_g^{-1}(v_a, v_b) \mathcal{R}e \left[ \mathcal{V}_{cg}(v_a) \mathcal{V}_{cg}^*(v_b) - \sum_i F_i(v_a) F_i(v_b) |\tilde{w}(\mathbf{U}_g - \mathbf{U}_i)|^2 \mathcal{V}_i(v_a) \mathcal{V}_i^*(v_b) \right] \quad (6)$$

where all the terms hold the same meaning as in TGE-I. The modified estimator in eq. (6) (hereafter referred to as TGE-II) differs from TGE-I in the second term within the square brackets. This term now subtracts out the self-correlation of a visibility with itself *i.e.* same baseline and timestamp considering all possible combinations of frequencies  $v_a$  and  $v_b$ . This removes the discontinuity at  $v_a = v_b$  in the estimated MAPS, and also avoids the negative bias in the estimated  $P(k)$ . We shall demonstrate this later in [Section 3.1](#), and we have validated TGE-II using simulations in [Section 4](#).

We now consider the normalization factor  $M_g(v_a, v_b)$ . Here we have used simulations to estimate the value of  $M_g(v_a, v_b)$ . We first simulate multiple realizations of a Gaussian random field having unit multi-frequency angular power spectrum (UMAPS;  $C_\ell(v_a, v_b) = 1$ ). We use this as the sky signal to simulate the corresponding visibilities  $[\mathcal{V}_i(v_a)]_{\text{UMAPS}}$  at the baselines and frequency channels identical to the data. The flagging of the actual data  $F_i(v_a)$  was applied to the simulated visibilities  $[\mathcal{V}_i(v_a)]_{\text{UMAPS}}$  and these are then analyzed identically to the actual data to obtain

$$M_g(v_a, v_b) = \mathcal{R}e \left[ \mathcal{V}_{cg}(v_a) \mathcal{V}_{cg}^*(v_b) - \sum_i F_i(v_a) F_i(v_b) |\tilde{w}(\mathbf{U}_g - \mathbf{U}_i)|^2 \mathcal{V}_i(v_a) \mathcal{V}_i^*(v_b) \right]_{\text{UMAPS}}. \quad (7)$$

We average over multiple realizations of the simulated UMAPS to reduce the statistical uncertainties in the estimated values of  $M_g(v_a, v_b)$ . For the subsequent analysis, we have simulated 50 realizations of UMAPS and used these to estimate  $M_g$ . Note that our estimator does not incorporate the migration of the baselines with frequency and considers the values of the baselines to be fixed at the reference frequency  $\nu_c$ .

The estimator in eq. (6) gives an unbiased estimate of the MAPS  $\langle \hat{E}_g(v_a, v_b) \rangle = C_{\ell_g}(v_a, v_b)$  at the grid point  $\mathbf{U}_g$ , or equivalently at angular multipole  $\ell_g = 2\pi |\mathbf{U}_g|$ . To increase the signal-to-noise ratio, we further bin the entire  $\ell$  range into 10  $\ell$  bins. The bin averaged Tapered Gridded Estimator is defined as,

$$\hat{E}_G[q](v_a, v_b) = \frac{\sum_g w_g \hat{E}_g(v_a, v_b)}{\sum_g w_g}, \quad (8)$$

where the sum is over all the grid points  $\mathbf{U}_g$  in the  $q$ 'th bin and the  $w_g$ 's are the corresponding weights. Here, we have used  $w_g = M_g(v_a, v_b)$  which implies that the weight is proportional to the baseline density of the particular grid point. The ensemble average of  $\hat{E}_G[q](v_a, v_b)$  gives an unbiased estimate of the bin averaged MAPS  $\bar{C}_{\bar{\ell}_q}(v_a, v_b)$  at the effective angular multipole  $\bar{\ell}_q = \frac{\sum_g w_g \ell_g}{\sum_g w_g}$ . Throughout this work we have considered baselines within  $U \leq 3000\lambda$  (equivalently,  $\ell \leq 18850$ ) and divided this into 10  $\ell$  bins. The effective angular multipoles corresponding to these bins cover a



range  $535 \lesssim \bar{\ell}_q \lesssim 15850$ . Note that  $\bar{\ell}_q$  vary slightly with the value of  $f$  and the values quoted in this paper have been estimated at  $f = 0.6$ . In the subsequent discussion we have used the simplified notation  $C_\ell(v_a, v_b)$  and  $\ell$  to denote  $\bar{C}_{\bar{\ell}_q}(v_a, v_b)$  and  $\bar{\ell}_q$  respectively.

Considering a sufficiently small bandwidth of observation, the redshifted 21-cm signal can be assumed to be statistically homogeneous (ergodic) along the line-of-sight (e.g. Mondal et al. 2019). This allows us to express  $C_\ell(v_a, v_b)$  in terms of  $C_\ell(\Delta\nu)$  where  $\Delta\nu = |v_b - v_a|$ . This means that the statistical properties of the signal can now be entirely described as a function of the frequency separations  $\Delta\nu$ . Under the flat sky approximation,  $P(k_\perp, k_\parallel)$  the 3D power spectrum of the 21-cm brightness temperature fluctuations is then given by the Fourier transform of  $C_\ell(\Delta\nu)$  along the line-of-sight (Datta et al. 2007),

$$P(k_\perp, k_\parallel) = r^2 r' \int_{-\infty}^{\infty} d(\Delta\nu) e^{-ik_\parallel r' \Delta\nu} C_\ell(\Delta\nu) \quad (9)$$

where  $k_\parallel$  and  $k_\perp = \ell/r$  are the components of  $\mathbf{k}$  respectively parallel and perpendicular to the line-of-sight,  $r$  and  $r' = dr/d\nu$  are respectively the comoving distance and its derivative with respect to  $\nu$ , both evaluated at the reference frequency  $\nu_c = 432.8$  MHz. Here  $r$  and  $r'$  are evaluated to have values 5703 Mpc and 9.85 Mpc/MHz respectively.

We use a maximum likelihood estimator to estimate the PS  $\bar{P}(k_\perp, k_\parallel)$  from the measured  $C_\ell(n\Delta\nu_c)$ , where  $n, m \in [0, N_E - 1]$  and  $N_E = N_c/2$ . Note that here we have used half of the available frequency separations  $0 \leq \Delta\nu \leq (N_c/2 - 1)\Delta\nu_c$  to avoid the poorly sampled higher frequency separations. In matrix notation,

$$C_\ell(n\Delta\nu_c) = \sum_m \mathbf{A}_{nm} \bar{P}(k_\perp, k_\parallel) + [\text{Noise}]_n \quad (10)$$

where  $\mathbf{A}_{nm}$  are the components of the  $N_E \times N_E$  Hermitian matrix  $\mathbf{A}$  containing the coefficients of the Fourier transform and  $[\text{Noise}]_n$  is an additive noise associated with each estimated  $C_\ell(n\Delta\nu_c)$ . The maximum likelihood estimate of  $\bar{P}(k_\perp, k_\parallel)$  is given by,

$$\bar{P}(k_\perp, k_\parallel) = \sum_n \{[\mathbf{A}^\dagger \mathbf{N}^{-1} \mathbf{A}]^{-1} \mathbf{A}^\dagger \mathbf{N}^{-1}\}_n \{ \mathcal{W}_{\text{BN}}(n\Delta\nu_c) C_\ell(n\Delta\nu_c) \} \quad (11)$$

where  $\mathbf{N}$  is the noise covariance matrix and ‘ $\dagger$ ’ denotes the Hermitian conjugate. We have also introduced a Blackman-Nuttall (BN; Nuttall 1981) window function  $\mathcal{W}_{\text{BN}}(n\Delta\nu_c)$  along the  $\Delta\nu$  to reduce any unwanted ripples in the estimated PS along  $k_\parallel$  arising due to the finite bandwidth of observation.

We have estimated  $\mathbf{N}$  through ‘noise-only’ simulations. As mentioned earlier, we have assumed that the noise in the visibilities are drawn from a Gaussian random distribution with zero mean and variance  $2\sigma_N^2$ , and are uncorrelated at different baselines, frequencies and timestamps. We have simulated visibilities corresponding to the system noise only at baselines and frequencies identical to the actual data along with the flagging statistics. We use the value of  $\sigma_N^2$  estimated from the data itself (Table 2). We apply our estimator (eq. 6) to estimate the MAPS corresponding to the simulated noise only visibilities. We generate multiple statistically independent noise-only visibility realizations to estimate the noise covariance matrix  $\mathbf{N}$  from the estimated MAPS. This method has been validated in Paper II. The reader is referred to Paper II for further details. Throughout the work, we have used 50 noise realizations to estimate the noise covariance matrix  $\mathbf{N}$ . Further, we have also estimated the PS  $P(k_\perp, k_\parallel)$  for each of these noise-only simulations, and we have determined the mean and variance  $[\delta P_N]^2$  of these values. As expected, the mean is consistent with zero. We have used  $[\delta P_N]$  to quantify the system

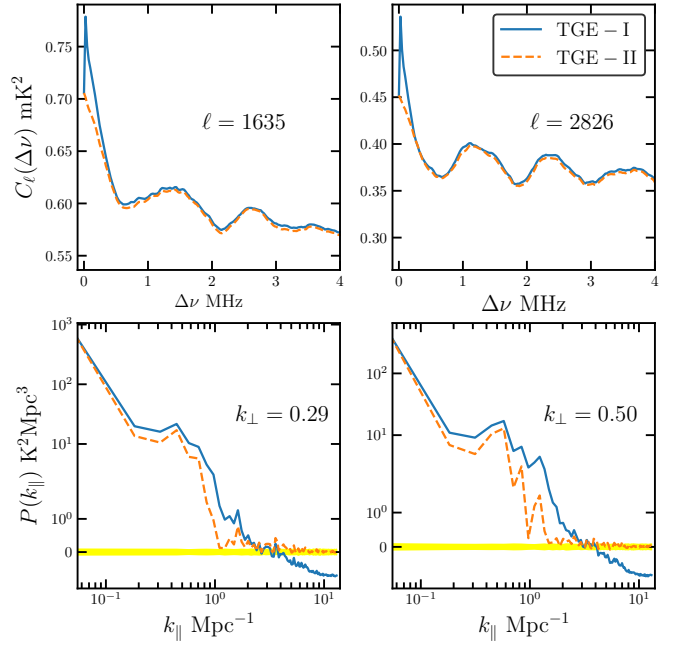


**Figure 2.** A comparison of TGE-I (blue solid lines) with TGE-II (orange dashed lines) applied on the combined nights data with  $f = 0.6$ . The upper panels show  $C_\ell(\Delta\nu)$  as a function of  $\Delta\nu$  for two different  $\ell$  values. The lower panels show slices of the estimated  $P(k_\perp, k_\parallel)$  as a function of  $k_\parallel$  at a fixed value of  $k_\perp$  corresponding to the  $C_\ell(\Delta\nu)$  shown in the upper panels. The yellow shaded regions show  $1\sigma$  errors  $\delta P_N$  due to system noise.

noise contribution to the statistical fluctuations of the estimated PS of the actual data.

We use eq. (11) to estimate of the 3D PS  $\bar{P}(k_\perp, k_\parallel)$  from the measured  $C_\ell(n\Delta\nu_c)$ . We have further binned  $\bar{P}(k_\perp, k_\parallel)$  along  $k_\parallel$  to obtain the bin averaged  $P(k_\perp, k_\parallel)$  which we present in the subsequent analysis. The estimated bin averaged cylindrical power spectra  $P(k_\perp, k_\parallel)$  span a  $(k_\perp, k_\parallel)$  range of  $0.09 \leq k_\perp \leq 2.78$  Mpc $^{-1}$  and  $0 \leq k_\parallel \leq 13.1$  Mpc $^{-1}$  respectively.

### 3.1 A comparison between TGE-I and TGE-II

In this sub-section, we briefly demonstrate the shortcoming of TGE-I (eq. 4) which was originally defined in Paper I, and we also show that these can be overcome by TGE-II (eq. 6) which we have used here. We apply both estimators to the combined nights data for the tapering parameter  $f = 0.6$ . The upper panels of Figure 2 show the estimated  $C_\ell(\Delta\nu)$  as a function of  $\Delta\nu$  for two  $\ell$  values for both TGE-I and TGE-II. We have restricted the frequency range to 4 MHz in the figure to highlight the abrupt discontinuity observed at  $\Delta\nu = 0$  for  $C_\ell(\Delta\nu)$  estimated with TGE-I. As discussed in Section 3, this dip arises due to the self-correlation term which is only subtracted for  $\nu_a = \nu_b$  to remove the noise bias. We see that the discontinuity is not present for TGE-II where we have subtracted out the self-correlation at all  $\Delta\nu$ . We also note that, as expected, the results from TGE-I and II both match for large  $\Delta\nu$ .

The lower panels of Figure 2 show slices of the PS  $P(k_\perp, k_\parallel)$  along  $k_\parallel$  at a fixed  $k_\perp$  estimated using eq. (11) from the  $C_\ell(\Delta\nu)$  shown in the upper panels. The yellow shaded regions show the  $1\sigma$  statistical fluctuations ( $\delta P_N$ ) arising due to system noise. In all cases  $P(k_\perp, k_\parallel)$  has relatively large values at small  $k_\parallel$  which correspond

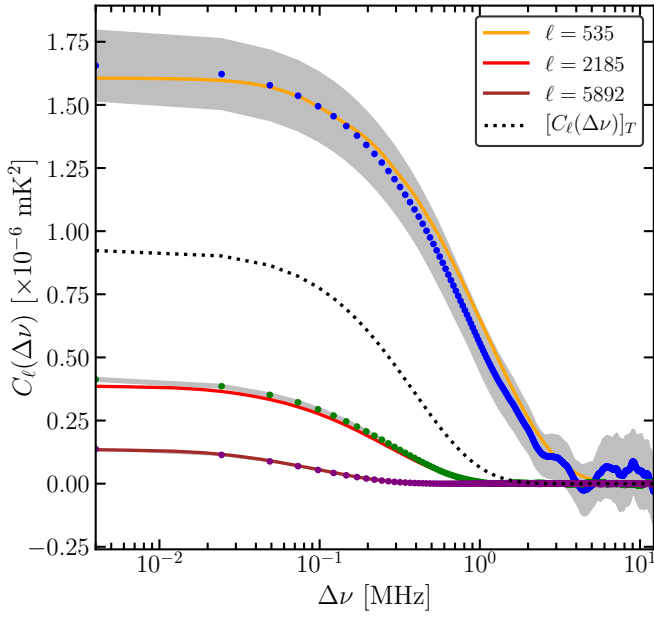


**Figure 3.** The data points show the mean  $C_\ell(\Delta\nu)$  with  $2\sigma$  errors (shaded region) estimated from 16 realizations of the simulated sky signal. We have restricted  $\Delta\nu$  to  $\leq 12.2$  MHz in the plot, which we have used to estimate the PS. The solid lines show the analytical predictions corresponding to the input model  $P^m(k)$ . The dotted line shows  $[C_\ell(\Delta\nu)]_T$  the cosmological 21-cm signal predicted at  $\ell = 1635$  for the  $\Lambda$ CDM model with  $[\Omega_{\text{H I}}, b_{\text{H I}}] = 10^{-3}$ . Note that the  $\Delta\nu = 0$  points are shifted slightly for plotting on a logarithmic scale.

to modes within the foreground wedge. The values of  $P(k_\perp, k_\parallel)$  fall with increasing  $k_\parallel$  up to  $k_\parallel \sim 4 \text{ Mpc}^{-1}$  beyond which the results from the two estimators are quite different. For TGE-I (blue solid line), in both the panels we notice that  $P(k_\perp, k_\parallel)$  has negative values for  $k_\parallel \gtrsim 4 \text{ Mpc}^{-1}$  and the values fall to  $\sim -0.8 \text{ K}^2 \text{ Mpc}^3$  at the largest  $k_\parallel$ -bins. In contrast, we find that this negative bias is absent in TGE-II (orange dashed lines) where the values of  $P(k_\perp, k_\parallel)$  oscillate around zero for  $k_\parallel \gtrsim 4 \text{ Mpc}^{-1}$ . Further, we also see that these oscillations are roughly within the yellow shaded region, indicating that these are consistent with the fluctuations expected from the system noise in the data. The negative bias in TGE-I arises from the abrupt dip at  $\Delta\nu = 0$  seen in  $C_\ell(\Delta\nu)$ . We have also noticed large negative values in  $P(k_\parallel)$  at a few grid points  $U_g$  for TGE-II near the wedge boundary. This is mostly originating due to a combination of corrupted baselines (most possibly due to bandpass calibration errors) at a few grid points. At these grid points we also observe a small dip near  $\Delta\nu = 0$  in  $C_\ell(\Delta\nu)$ . At this stage, we have decided to flag these grid points, favouring less data rather than bad data. Typically about  $\sim 17\%$  of grid points are flagged. We see that the negative bias is not present for TGE-II after the flagging (Figure 2), and we use the rest of the grid points for further analysis. We also drop the suffix “-II” and refer to this as TGE throughout the rest of the Paper.

#### 4 SIMULATION

We have already validated TGE in Paper II using 150 MHz GMRT simulations where  $\sim 47\%$  of the data were flagged. We found that TGE could recover the input PS with  $< 8\%$  fractional deviation over the entire  $k$ -range used for the analysis. In the present work, we have

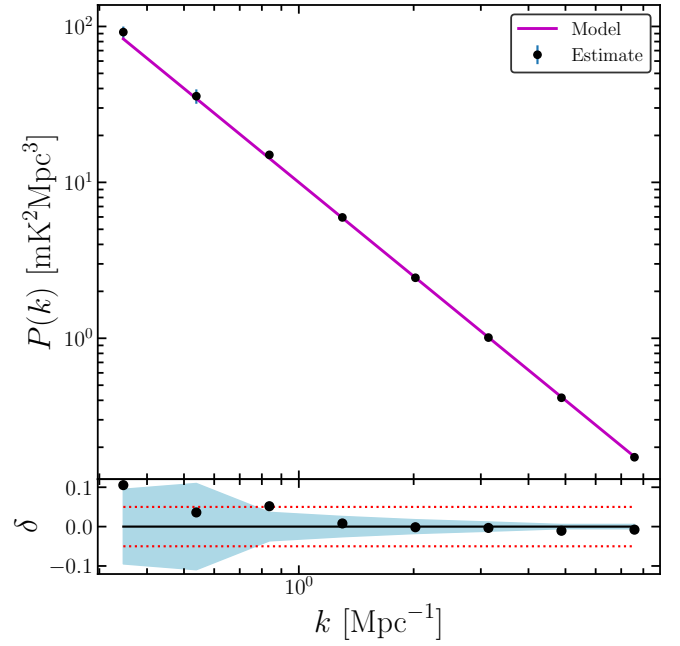


**Figure 4.** The upper panel shows the estimated spherically-binned power spectrum  $P(k)$  (data points) and  $2\sigma$  error-bars for the simulations along with the input model  $P^m(k)$  (purple solid line). The bottom panel shows the fractional deviation  $\delta = [P(k) - P^m(k)]/P^m(k)$  (data points) and the expected  $2\sigma$  statistical fluctuations for the same (blue shaded region). The (red) dotted lines demarcate the region where  $|\delta| \leq 0.05$ .

repeated a similar analysis for the sub-band 2 data, which we have analyzed here. The aim is to validate the estimator and quantify the accuracy to which TGE is expected to recover  $P(k)$  for the data analyzed here.

The 21-cm brightness temperature fluctuations  $\delta T_b(\hat{n}, \nu)$  in the simulations are assumed to be a Gaussian random field corresponding to an input model

$$P^m(\mathbf{k}) = A \left( \frac{k}{k_0} \right)^n \text{ mK}^2 \text{ Mpc}^3. \quad (12)$$

where we have arbitrarily set  $A = 10$ ,  $k_0 = 1 \text{ Mpc}^{-1}$ , and used a power law index  $n = -2$ . The simulations closely follow the prescriptions of Choudhuri et al. (2016b) and Paper II. We have carried out simulations on a  $N^3 = [1024]^3$  cubic grid with a grid spacing  $\Delta L = 0.24 \text{ Mpc}$  which matches the spectral resolution  $\Delta\nu_c = 24.4 \text{ kHz}$  of our data ( $\Delta L = r' \times \Delta\nu_c$ ). This results in an angular resolution of  $\Delta\theta \sim 8.4''$  ( $\Delta L = r\Delta\theta$ ), and the angular extent of the simulation box ( $N\Delta\theta$ ) covers  $\sim 2.5$  times the  $\theta_{\text{FWHM}}$  of GMRT at the frequency  $\nu_c = 432.8 \text{ MHz}$ . We have converted the simulated images into visibilities using the baseline distribution of the combined nights data. The simulations incorporate the frequency dependence of the PB and baseline migration.

We have applied the TGE (eq. 6) on the simulated visibilities, and analyzed the simulated data identical to the actual data, to estimate the MAPS  $C_\ell(\Delta\nu)$ . We have used  $N_r = 16$  independent realizations of the simulation to estimate the mean  $C_\ell(\Delta\nu)$  and the  $2\sigma$  errors shown in Figure 3 at three values of  $\ell$  for  $f = 0.6$ . We have also shown (solid lines) the analytical model predictions  $C_\ell^m(\Delta\nu)$  calculated using (Datta et al. 2007; Ali & Bharadwaj 2014)

$$C_\ell(\Delta\nu) = \frac{1}{\pi r^2} \int_0^\infty dk_\parallel \cos(k_\parallel r' \Delta\nu) P(\mathbf{k}). \quad (13)$$

We see that the  $C_\ell(\Delta\nu)$  estimated from the simulations closely matches the analytical prediction  $C_\ell^m(\Delta\nu)$  which are mostly within the shaded region showing the  $2\sigma$  uncertainty. The deviations between  $C_\ell(\Delta\nu)$  and  $C_\ell^m(\Delta\nu)$  are found to lie within  $\lesssim 10\%$  at  $\Delta\nu = 0$ . These deviations are primarily due to uncertainties in the normalization factors  $M_g(\nu_a, \nu_b)$  which have been estimated from 50 UMAPS realizations. To test this we have checked that these deviations decrease if the number of UMAPS realizations is increased. We also note that the large  $\Delta\nu$  are poorly sampled compared to the small  $\Delta\nu$ , and the cosmic variance increases as we go to larger frequency separations.

The dotted line in Figure 3 shows  $[C_\ell(\Delta\nu)]_T$  an estimate of the cosmological 21-cm signal expected in the observed data. It is assumed that the fluctuations of the H I distribution trace the underlying matter distribution with a linear bias  $b_{\text{H I}}$ . This allows us to express  $P_T(\mathbf{k})$  the predicted 21-cm brightness temperature power spectrum in terms of  $P_m^s(\mathbf{k})$  the underlying matter power spectrum in redshift space. Here we have rewritten eq. (23) of Bharadwaj & Ali (2005) as

$$P_T(\mathbf{k}) = [\Omega_{\text{H I}} b_{\text{H I}}]^2 \bar{T}^2 P_m^s(\mathbf{k}) \quad (14)$$

with

$$\bar{T}(z) = 133 \text{ mK} (1+z)^2 \left(\frac{h}{0.7}\right) \left(\frac{H_0}{H(z)}\right) \quad (15)$$

where the cosmological H I mass density  $\Omega_{\text{H I}}$  is the comoving H I mass density in units of the present critical density. DLA observations (e.g. Noterdaeme et al. 2012; Zafar et al. 2013) show that  $\Omega_{\text{H I}} \sim 10^{-3}$  across  $1.5 < z < 5$ , whereas various simulations (e.g. Sarkar et al. 2016) indicate  $1 \leq b_{\text{H I}} \leq 2$  across ( $2 \leq z \leq 3$ ). For the estimates presented here we have used  $[\Omega_{\text{H I}} b_{\text{H I}}] = 10^{-3}$  and a fitting formula for  $P_m(k)$  (Eisenstein & Hu 1998), ignoring the effect of redshift space distortion. We find that  $[C_\ell(\Delta\nu)]_T$  has a peak value of  $\approx 0.9 \times 10^{-6} \text{ mK}^2$  at  $\Delta\nu = 0$  for the value of  $\ell$  ( $= 1635$ ) shown here. The value of  $[C_\ell(\Delta\nu)]_T$  decreases with increasing  $\Delta\nu$  and it is  $\approx 0$  for  $\Delta\nu > 1 \text{ MHz}$ . In fact, a similar behaviour is also seen for the model predictions  $[C_\ell^m(\Delta\nu)]$  where we find that the value peaks at  $\Delta\nu = 0$  and decorrelates rapidly with increasing  $\Delta\nu$  with a value  $\approx 0$  at  $\Delta\nu > 1 \text{ MHz}$ . The peak value reduces with increasing  $\ell$  for which the signal also decorrelates faster. These are generic features of the expected 21-cm signal (Bharadwaj & Pandey 2003) irrespective of the details of the 21-cm PS.

We have implemented eq. (11) to estimate the PS of the simulated sky signal. Identical to the actual data, we have also used a BN window function along the frequency separation for these simulations. The simulations differ from the data in that the error-covariance  $\mathbf{N}$  is dominated by cosmic variance, whereas the data is system noise dominated. Here we have used the covariance of the simulated  $C_\ell(\Delta\nu)$  to estimate the noise covariance matrix  $\mathbf{N}$ . The upper panel of Figure 4 shows the estimated spherically-binned PS  $P(k)$  and the associated  $2\sigma$  errors along with the model PS  $P^m(k)$ . We see that  $P(k)$  is in reasonably good agreement with  $P^m(k)$  across the entire  $k$  range considered here. The lower panel of Figure 4 shows the fractional deviation  $\delta = [P(k) - P^m(k)]/P^m(k)$  and the expected  $2\sigma$  statistical fluctuations for the same. We have  $|\delta| \lesssim 5\%$  in most of the  $k$ -bins shown here. We have somewhat larger deviation ( $|\delta| \sim 10\%$ ) at the smallest  $k$ -bin. The convolution with the window function (eq. 3) is expected to become important at the small baselines (Choudhuri et al. 2014), and this possibly contributes to enhance the deviations in the small  $k$ -bins. A part of the deviations could also arise from the low baseline density in some of the bins (Figure 1). We see that the  $\delta$  values are all consistent with the predicted  $2\sigma$  errors. In the

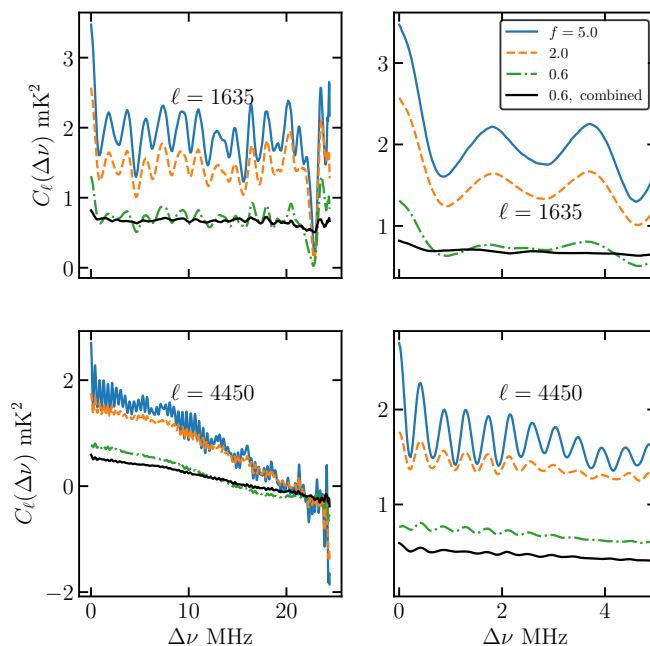


**Figure 5.**  $C_\ell(\Delta\nu)$  as a function of  $\Delta\nu$  for the May 6 observation are shown at  $f = 5.0, 2.0$ , and  $0.6$  at two values of the angular multipole  $\ell$ . The left panels show the  $C_\ell(\Delta\nu)$  for the entire 24.4 MHz bandwidth considered here. The right panels show the same but we restrict the frequency separation upto 5 MHz. The black solid lines represent the estimated  $C_\ell(\Delta\nu)$  using  $f = 0.6$  for the combined data.

analysis of the actual observed data, as presented later in this paper, we have identified some of the  $(k_\perp, k_\parallel)$  modes as being foreground contaminated. These modes have been excluded for estimating the spherically-binned PS  $P(k)$  of the actual data. In keeping with this, we have also excluded these modes for the simulations presented here. The entire validation presented here used *exactly* the same  $(k_\perp, k_\parallel)$  modes as those that have been used for the actual data. In summary, we have validated the TGE and we find that it is able to recover the input model PS to an accuracy better than  $\lesssim 10\%$  across the entire  $k$  range considered here, and  $\lesssim 5\%$  across  $0.54 \leq k \leq 7.58 \text{ Mpc}^{-1}$ . The results are not very different even if we include all the available  $(k_\perp, k_\parallel)$  modes to estimate  $P(k)$ .

## 5 RESULTS

### 5.1 The Estimated MAPS

We have used the TGE (eqs. 6 and 8) to estimate the MAPS  $C_\ell(\Delta\nu)$  from the calibrated and compact source subtracted visibility data for the individual nights of observation as well as the combined data. We see that the May 6 data (Table 2) has the least flagging as well as the smallest visibility r.m.s. Guided by this, we first consider the results for the May 6 data and subsequently use this as a reference for comparing the results for the other nights (not shown here) and the combined data. The two polarizations (LL and RR) were treated as independent measurements from the same baseline. We have repeated the analysis for three values of the tapering parameter  $f = 5.0, 2.0$ , and  $0.6$ . As mentioned earlier, the tapering increases with decreasing value of  $f$ , and  $f = 5.0$  can be considered equivalent to an untapered PB.

In Figure 5 we have shown  $C_\ell(\Delta\nu)$  as a function of the frequency

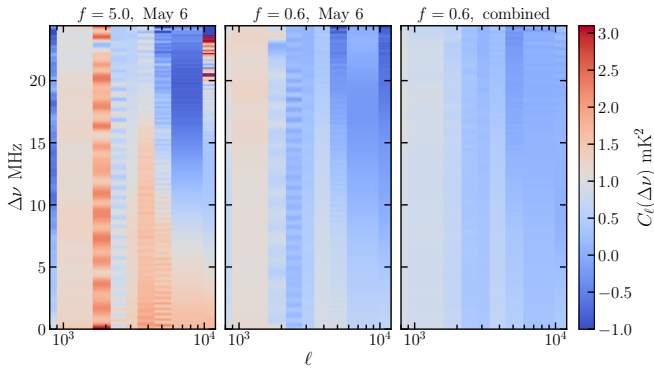


**Figure 6.** This shows  $C_\ell(\Delta\nu)$  across the entire  $(\ell, \Delta\nu)$  range for May 6 at  $f = 5$  (left panel), May 6 at  $f = 0.6$  (middle panel) and four nights combined data at  $f = 0.6$  (right panel).

separation  $\Delta\nu$  at different values of  $f$  for the May 6 data. The upper and lower panels correspond to two representative  $\ell$ -values,  $\ell = 1635$  and  $4450$  respectively. The left and right panels show  $C_\ell(\Delta\nu)$  over the entire 24.4 MHz bandwidth and  $\Delta\nu \leq 5$  MHz respectively. We see that  $C_\ell(\Delta\nu)$  exhibit an oscillatory pattern whose frequency increases with  $\ell$ . This increase in the frequency of oscillation is more evident in the right panels which show a small part of the  $\Delta\nu$  range. These oscillatory patterns are consistent with the expected foreground behaviour (Ghosh et al. 2011a,b, 2012). The contribution to  $C_\ell(\Delta\nu)$  from a single point source is predicted (Paper II) to be

$$C_\ell(\Delta\nu) \propto \cos(\ell\theta\Delta\nu/\nu_c) \quad (16)$$

where  $\theta$  is the sine of the angle between the source position and the phase center of the observation. As mentioned earlier, the compact and discrete sources within the main lobe of the PB have been modelled and subtracted out (Chakraborty et al. 2019b). However, far-field residual sources remain that are difficult to model and clean out from the data. The oscillations in the estimated  $C_\ell(\Delta\nu)$  is essentially a superposition of the oscillatory contributions from all the residual sources outside the main lobe of the PB. Note that the oscillation in  $C_\ell(\Delta\nu)$  is fundamentally due to the chromatic nature of radio-interferometric measurements. The increase in the frequency of oscillation in  $C_\ell(\Delta\nu)$  at larger baselines yields the ‘wedge’ shape in the PS, which we shall present shortly. The extent of this ‘foreground wedge’ is determined by the position ( $\theta$ ) of the wide-field source, which can maximally reach the horizon limit  $\theta \sim 1$ . The oscillations seen here, or equivalently the foreground wedge, arises due to ‘baseline migration’ (Datta et al. 2010; Morales et al. 2012; Parsons et al. 2012; Vedantham et al. 2012; Murray & Trott 2018). TGE allows us to suppress the antenna response at large angular distances relative to the phase center, reducing the large angular-scale foreground contributions present in the data. This is illustrated in Figure 5 where we see that for both the  $\ell$  values the overall amplitude of  $C_\ell(\Delta\nu)$  goes down as the value of  $f$  is reduced (or equivalently, the tapering is increased). Comparing with respect to  $f = 5.0$ , we find that the amplitude of  $C_\ell(0)$  drops by a factor 3 – 4 for  $f = 0.6$  at the  $\ell$  values shown here. Further, the amplitude of the oscillatory pattern also decreases considerably as the value of  $f$  is reduced. The implication of this on the PS will be discussed in Section 5.2 where we consider the PS for different values of  $f$ .

Figure 6 shows  $C_\ell(\Delta\nu)$  across the entire  $(\ell, \Delta\nu)$  range. A comparison of the results obtained from the May 6 data with  $f = 5.0$  (left panel) and  $f = 0.6$  (middle panel) demonstrates the effect of taper-

ing. Considering the left panel, we see that the oscillations along  $\Delta\nu$  are prominently visible in most of the  $\ell$ -bins. For larger  $\ell$ , the oscillations become so rapid that we cannot discern them in the figure. The overall amplitude and that of the oscillatory pattern are both visibly reduced in the middle panel. The rightmost panel shows  $C_\ell(\Delta\nu)$  for the combined nights data for  $f = 0.6$ . It is evident from the last two panels of the Figure 6 that combining different nights data yields a further smoothing of the oscillatory patterns. This is also illustrated in Figure 5 which shows  $C_\ell(\Delta\nu)$  for the combined data in black-solid lines for  $f = 0.6$ . We see, in both the Figures 5 and 6, that the overall amplitude of  $C_\ell(\Delta\nu)$  as well as the amplitude of the oscillations are smaller for the combined nights in comparison to the May 6 data. The reason is that the convolution (eq. 3), which incorporates the tapering in TGE, is sensitive to the baseline distribution (Choudhuri et al. 2014). The baseline densities for May 6 and the combined nights are shown in the lower panels of Figure 1. We see that the baseline density increases by a factor  $\sim 3.5$  for the combined nights data. The uv-coverage is also considerably less patchy in comparison to the May 6 data. We expect the tapering to be more effective for the denser and more uniform baseline coverage of the combined nights. We see that this expectation is borne out in the estimated  $C_\ell(\Delta\nu)$ .

In addition to the rapid oscillations in  $C_\ell(\Delta\nu)$  (Figures 5 and 6) which arise from the residual compact source contribution due to baseline migration,  $C_\ell(\Delta\nu)$  also exhibits a gradual de-correlation *i.e.* the value of  $C_\ell(\Delta\nu)$  decreases as  $\Delta\nu$  increases. We expect the intrinsic frequency spectrum of the compact sources to cause a smooth de-correlation of  $C_\ell(\Delta\nu)$ . However, it is interesting to note that the values of  $C_\ell(\Delta\nu)$  do not fall monotonically with increasing  $\Delta\nu$ . We can observe this in the lower left panel of Figure 5 where the amplitude of the oscillations in  $C_\ell(\Delta\nu)$  decreases till  $\Delta\nu \sim 5$  MHz, then increases again up to  $\Delta\nu \sim 10$  MHz, and then decreases again. This modulation, we believe, arises because of the PB pattern which changes with frequency across the frequency bandwidth considered here. The position of the null points of the PB changes considerably with frequency, and this possibly causes the slow modulation seen in  $C_\ell(\Delta\nu)$ .

## 5.2 The Estimated PS

We have applied the maximum likelihood method described in Section 3 on  $C_\ell(\Delta\nu)$  to estimate the cylindrical power spectra  $P(k_\perp, k_\parallel)$ . The different panels of Figure 7 show the absolute values of the PS. The first three panels, starting from the left, respectively correspond to  $f = 5.0, 2.0,$  and  $0.6$  for the May 6 data while the right panel corresponds to  $f = 0.6$  for the combined nights. In all cases, the foregrounds are found to be largely confined within a wedge in the  $(k_\perp, k_\parallel)$  plane. The wedge boundary (also called the ‘horizon limit’) can be mapped to a straight line  $[k_\parallel]_H = (r/r'\nu_c)k_\perp$  in the  $(k_\perp, k_\parallel)$  plane (Pober et al. 2016). The region  $k_\parallel \leq [k_\parallel]_H$  is referred to as the ‘foreground wedge’, and the PS estimated in this region of the  $(k_\perp, k_\parallel)$  plane is largely dominated by the foregrounds. The region  $k_\parallel > [k_\parallel]_H$  is relatively foreground-free, and we refer to this as the ‘21-cm window’. While the bulk of the foregrounds in Figure 7 are localized within the foreground wedge, all the panels also show some foreground leakage outside the predicted wedge boundary. Various factors like the chromaticity of the sky signal and the PB, sparse sampling of baselines, calibration errors, etc., cause this foreground to leak into the 21-cm window (Bowman et al. 2009; Thyagarajan et al. 2016), and it is often necessary to discard a part of the 21-cm window for estimating the PS of the 21-cm signal.

We now compare the PS values in the three left panels of Figure 7 which respectively correspond to  $f = 5.0, 2.0$  and  $0.6$  for the May 6



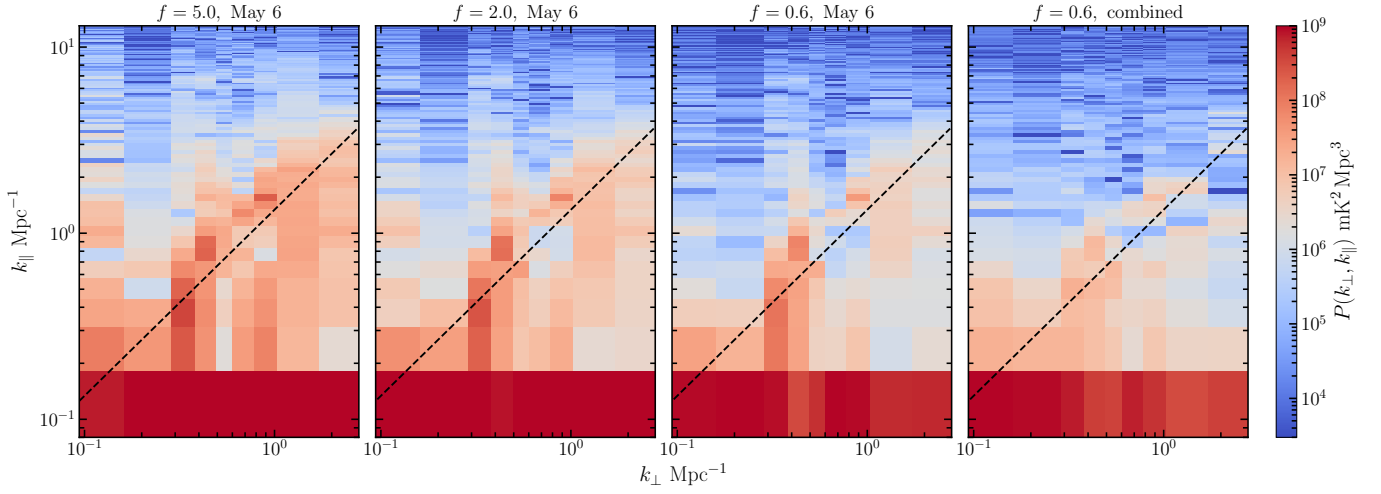


**Figure 7.** The first three panels from the left show the absolute values of the cylindrical power spectra  $P(k_{\perp}, k_{\parallel})$  for the May 6 data for different values of tapering. The rightmost panel shows the same for the combined nights data for  $f = 0.6$ . In all the cases the black dashed lines denote  $[k_{\parallel}]_H$ .

data. We see that the overall foreground contamination comes down as the value of  $f$  is reduced *i.e.* the tapering is increased, and we have a larger side-lobe suppression. In addition to a decrease in amplitude within the foreground wedge, we also notice a reduction in the leakage outside the wedge. However, this effect is not uniform across the different  $k_{\perp}$ -bins. The convolution which incorporates the tapering is expected to be more effective when we have a denser and more uniform  $uv$  coverage of the baselines. As discussed in Section 5.1, we have a denser baseline distribution at the small baselines, which is reflected in the fact that the foreground suppression is more effective at the lower  $k_{\perp}$ -bins. The rightmost panel of Figure 7 corresponds to  $f = 0.6$  for the combined nights data. Comparing the two rightmost panels, both of which correspond to  $f = 0.6$ , we see that we have a smaller foreground contribution for the combined nights data compared to the May 6 data. This is expected because the combined nights data has a  $\sim 3.5$  times larger baseline density in comparison to the May 6 data (Figure 1). We see that we have the lowest level of foreground contribution for the combined nights data with  $f = 0.6$ , and we have focused on this for the subsequent analysis of this paper.

We next consider the estimated values of  $P(k_{\perp}, k_{\parallel})$  in some detail. To study this, in Figure 8 we have shown the absolute values of  $P(k_{\perp}, k_{\parallel})$  as a function of  $k_{\parallel}$  for two different fixed  $k_{\perp}$  bins corresponding to  $k_{\perp} = 0.50 \text{ Mpc}^{-1}$  (upper panel) and  $0.78 \text{ Mpc}^{-1}$  (lower panel). The results are shown for the combined nights data, considering two values of tapering namely  $f = 5.0$  and  $f = 0.6$ . In each panel, the vertical red solid line denotes  $[k_{\parallel}]_H$  which is the predicted foreground wedge boundary for the particular  $k_{\perp}$ -bin. Further, the shaded region denotes the predicted  $1\sigma$  errors ( $[\delta P_N]$ ) due to the system noise contribution considering  $f = 5.0$  (green) and  $0.6$  (light-blue). In all cases we have the largest value of  $P(k_{\perp}, k_{\parallel})$  ( $\sim 10^9 \text{ mK}^2 \text{ Mpc}^3$ ) at  $k_{\parallel} = 0$ . The value of  $P(k_{\perp}, k_{\parallel})$  falls ( $\sim 10^6 - 10^7 \text{ mK}^2 \text{ Mpc}^3$ ) till  $k_{\parallel}$  approaches  $[k_{\parallel}]_H$  where it flattens out, and then rises slightly in a few  $k_{\parallel}$  bins just beyond  $[k_{\parallel}]_H$ . Further beyond this, the value of  $|P(k_{\perp}, k_{\parallel})|$  falls with increasing  $k_{\parallel}$ . We find  $|P(k_{\perp}, k_{\parallel})| \sim 10^4 - 10^5 \text{ mK}^2 \text{ Mpc}^3$  at the largest  $k_{\parallel}$  bins where the power oscillates between positive and negative values which are comparable with the  $1 - \sigma$  error-bars. We interpret the estimated power in this region to be arising due to a combination of system noise and some residual foreground leakage. In both the

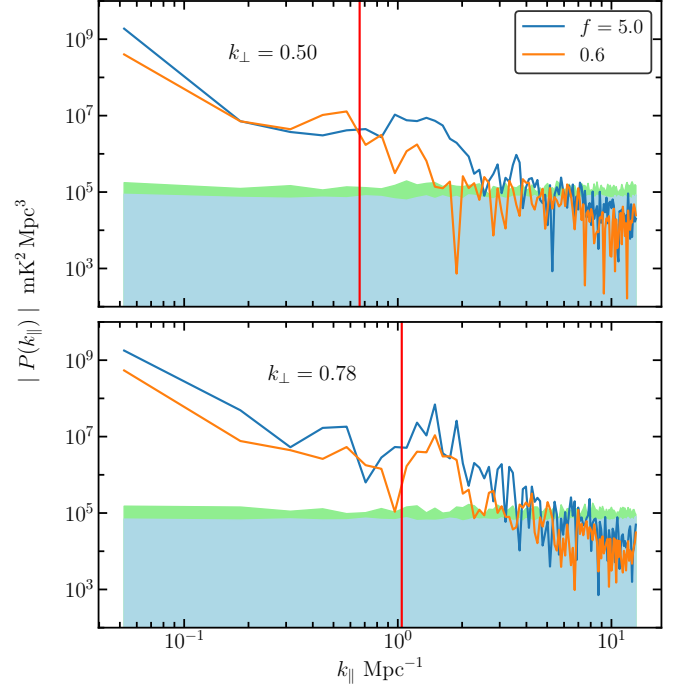


**Figure 8.** The absolute values of the cylindrical power spectra  $P(k_{\perp}, k_{\parallel})$  for the combined nights data are shown as a function of  $k_{\parallel}$  for  $f = 5.0$  and  $0.6$  at two representative values of  $k_{\perp}$ . The value at  $k_{\parallel} = 0$  has been slightly shifted for plotting on a log scale. The vertical red solid line denotes  $[k_{\parallel}]_H$  at the respective  $k_{\perp}$ -bin. The green and light-blue shaded regions show the  $1\sigma$  errors  $[\delta P_N]$  due to the system noise estimated at  $f = 5.0$  and  $0.6$  respectively.

panels we find that the values of  $|P(k_{\perp}, k_{\parallel})|$  decrease when  $f$  is reduced from  $f = 5.0$  to  $f = 0.6$ .

Considering Figure 8, as noted earlier, we find that there is a  $k_{\parallel}$  range within the foreground wedge where  $P(k_{\perp}, k_{\parallel})$  has a relatively small value in comparison to the values at  $k_{\parallel} = 0$  and  $k_{\parallel} \approx [k_{\parallel}]_H$ . This is also seen in the various panels of Figure 7 where we see

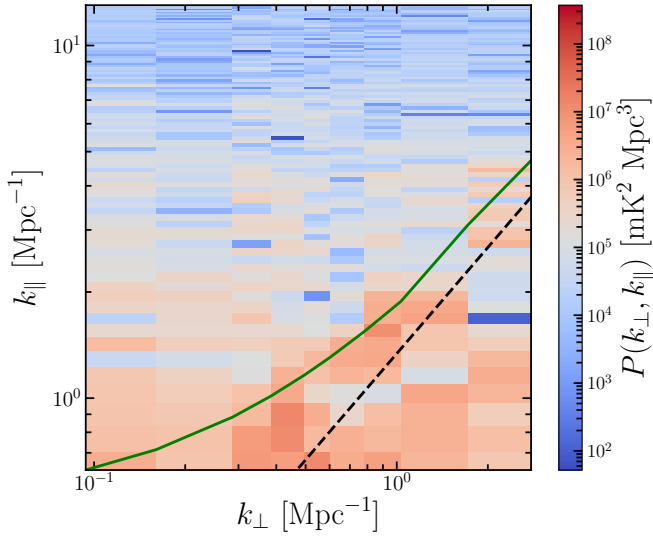


**Figure 9.** The cylindrical power spectra  $|P(k_{\perp}, k_{\parallel})|$  for the combined nights data for  $f = 0.6$ . Here the black-dashed line denotes  $[k_{\parallel}]_H$ . The region above the green solid line has been used for spherical binning.

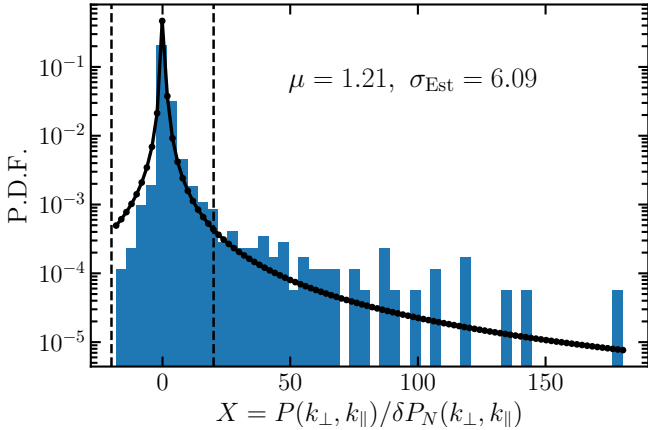


**Figure 10.** The histogram of the variable  $X = \frac{P(k_{\perp}, k_{\parallel})}{\delta P_N(k_{\perp}, k_{\parallel})}$ . The black-solid curve shows the fit with t-distribution. The mean 1.21 and standard deviation 6.09 are obtained from  $|X| \leq 20$ , demarcated by the vertical black-dashed lines.

that the values of  $P(k_{\perp}, k_{\parallel})$  fall as we move away from  $k_{\parallel} = 0$  and then increases again at  $k_{\parallel} \approx [k_{\parallel}]_H$ . We identify the rise in  $P(k_{\perp}, k_{\parallel})$  close to the horizon limit as a wide-field foreground effect known as the “pitchfork effect” (Thyagarajan et al. 2015a,b). The pitchfork effect has been previously reported in observations with the MWA (Thyagarajan et al. 2015b), PAPER (Kohn et al. 2016) and LOFAR (Gehlot et al. 2018) telescopes at lower frequencies ( $\sim 150$  MHz) which target the redshifted 21-cm signal from the Epoch of Reionization ( $z > 6$ ). The present work is possibly the first time this effect is being observed at higher frequencies which correspond to the post-reionization 21-cm signal. We notice (Figure 7) that the magnitude of the pitchfork effect is reduced as the tapering parameter is reduced from  $f = 5$  to  $f = 0.6$ .

Figure 9 shows the best results for the cylindrical PS  $|P(k_{\perp}, k_{\parallel})|$  which has been used to estimate the spherically binned PS  $P(k)$

where  $k = \sqrt{k_{\perp}^2 + k_{\parallel}^2}$ . This has been obtained from the combined nights data for  $f = 0.6$ . The black dashed line shows  $[k_{\parallel}]_H$  the predicted boundary of the foreground wedge. We notice that the foreground leakage extends beyond  $[k_{\parallel}]_H$ . We have selected the entire  $k_{\perp}$  range, and  $k_{\parallel}$  modes inside the “21-cm window”, with a buffer region of  $0.5 - 1.0$   $\text{Mpc}^{-1}$  outside the wedge boundary as shown in Figure 9. We have included all the modes beyond the green solid lines in the  $(k_{\perp}, k_{\parallel})$  plane for the spherical binning. Figure 10 shows the statistics of the estimated  $P(k_{\perp}, k_{\parallel})$  for the selected region through a variable ‘X’, which is defined by the ratio of the PS to the statistical error due to the system noise at a  $(k_{\perp}, k_{\parallel})$ ,

$$X = \frac{P(k_{\perp}, k_{\parallel})}{\delta P_N(k_{\perp}, k_{\parallel})}. \quad (17)$$

We see that the probability density function (P.D.F.) is mostly symmetric within  $|X| \leq 20$  (area demarcated by the vertical black-dashed lines) with mean  $mean(X) = \mu = 1.21$  and  $\sqrt{var(X)} = \sigma_{Est} = 6.09$ . The negative values of  $X$  are consistent with roughly 3 times  $\sigma_{Est}$ , and no negative values are observed outside  $|X| \leq 20$ . This, along with the positive mean within this region, indicate that no negative bias can arise from the modes selected here for the spherical binning. Further, in the scenario where the PS in the selected region are solely dominated by the system noise which follows a Gaussian distribution with zero mean and variance  $\sigma_N^2$ , we expect the variable  $X$  to follow a Gaussian distribution with  $mean(X) = \mu$  and variance  $var(X) = \sigma_{Est}^2$  as estimated from a sample of  $N$ -points, with  $\mu$  being comparable to  $\frac{\sigma_{Est}}{\sqrt{N}}$  (i.e.  $\mu \lesssim \frac{\sigma_{Est}}{\sqrt{N}}$ ), and as  $N \rightarrow \infty$ ,  $\sigma_{Est}^2 \rightarrow 1$ . The standard deviation  $\sigma_{Est} > 1$  suggests that the estimated r.m.s. statistical fluctuations  $\delta P_N(k_{\perp}, k_{\parallel})$  are underestimated by a factor  $\sigma_{Est}$ . We note that factors such as RFI, residual point source contributions, residual calibration errors etc., can additionally contribute to the error and may have caused the variance to exceed the predicted value estimated from the system noise only. We account for this underestimation by multiplying the  $\delta P_N(k_{\perp}, k_{\parallel})$  with  $\sigma_{Est}$  henceforth to denote the actual error due to statistical fluctuations,  $\delta P_N^{True}(k_{\perp}, k_{\parallel}) = \sigma_{Est} \times \delta P_N(k_{\perp}, k_{\parallel})$ . The black-solid curve in Figure 10 shows the P.D.F. fitted with a t-distribution. We find that the P.D.F. is well described by the t-distribution within  $|X| \lesssim 20$ ; however, the long positive tail observed at higher  $X$  is not modelled well and is somewhat underestimated by the t-distribution function. From these observations, we interpret that the estimated  $P(k_{\perp}, k_{\parallel})$  contain contributions from statistical fluctuations as well as residual foreground emission in the region considered here. Note that we have considered  $(k_{\perp}, k_{\parallel})$  modes up to  $\frac{P(k_{\perp}, k_{\parallel})}{\delta P_N^{True}(k_{\perp}, k_{\parallel})} \approx 30$  for the spherical binning.

We have estimated the spherically binned PS  $P(k)$  using the cylindrical PS  $P(k_{\perp}, k_{\parallel})$  values in all the  $(k_{\perp}, k_{\parallel})$  modes which lie beyond the green solid line in Figure 9. The entire  $k$  range has been divided into 8 equally spaced logarithmic bins. The solid blue line in Figure 11 shows  $|\Delta^2(k)|$  where  $\Delta^2(k) \equiv k^3 P(k)/2\pi^2$  the estimated mean squared brightness temperature fluctuations along with the  $2\sigma$  error bars. Here  $\sigma = k^3 [\delta P_N^{True}(k)]/2\pi^2$ , where  $[\delta P_N^{True}(k)]$  is the r.m.s. estimated using the spherically binned PS from 50 realisations of noise only simulations multiplied by  $\sigma_{Est} = 6.09$ . The values of  $\Delta^2(k)$  and  $\sigma$  are tabulated in Table 3 for reference. Considering the values of  $\Delta^2(k)$ , we find that this has the smallest value  $\Delta^2(k) = (128.91)^2 \text{ mK}^2$  for the first bin at  $k = 0.347 \text{ Mpc}^{-1}$ . The value of  $\Delta^2(k)$  increases approximately as  $\Delta^2(k) = (244.16)^2 \text{ mK}^2 (k/1\text{Mpc}^{-1})$  in the entire  $k$  range  $0.347 < k < 7.584 \text{ Mpc}^{-1}$ . The values of  $\Delta^2(k)$  in all of the first

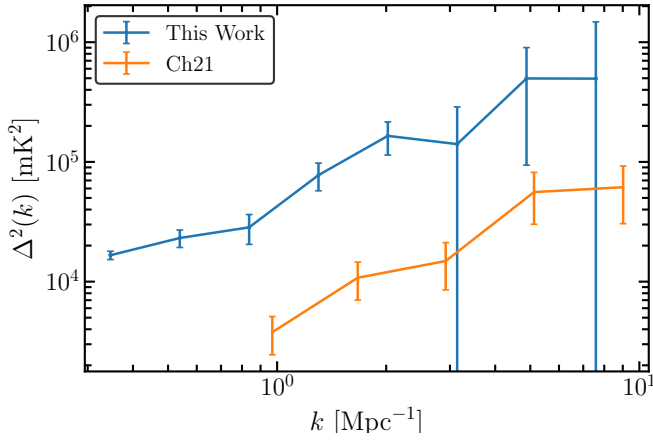


**Figure 11.** The mean square brightness temperature fluctuations  $\Delta^2(k)$  shown as a function of  $k$  along with  $2\sigma$  error bars for the selected regions shown in Figure 9. The orange line shows the result at  $z = 2.19$  from Ch21 along with  $2\sigma$  error bars as reported in the paper.

**Table 3.** Spherically binned mean square brightness temperature fluctuations  $\Delta^2(k)$  and the corresponding statistical error predictions  $\sigma$  for different  $k$ -bins. The  $2\sigma$  upper limits  $\Delta_{UL}^2(k) = \Delta^2(k) + 2\sigma$  and corresponding  $[\Omega_{\text{H}_1} b_{\text{H}_1}]_{UL}$  values are also provided.

$k$ Mpc $^{-1}$	$\Delta^2(k)$ (mK) $^2$	$1\sigma$ (mK) $^2$	$\Delta_{UL}^2(k)$ (mK) $^2$	$[\Omega_{\text{H}_1} b_{\text{H}_1}]_{UL}$
0.347	(128.91) $^2$	(25.79) $^2$	(133.97) $^2$	0.230
0.539	(152.14) $^2$	(43.92) $^2$	(164.33) $^2$	0.234
0.837	(168.54) $^2$	(62.99) $^2$	(190.64) $^2$	0.230
1.301	(278.48) $^2$	(100.37) $^2$	(312.57) $^2$	0.326
2.021	(406.20) $^2$	(159.58) $^2$	(464.68) $^2$	0.425
3.141	(375.19) $^2$	(271.49) $^2$	(536.83) $^2$	0.436
4.881	(705.60) $^2$	(449.38) $^2$	(949.61) $^2$	0.694
7.584	(704.35) $^2$	(701.07) $^2$	(1216.18) $^2$	0.807

five bins and the seventh  $k$ -bin are well in excess of  $0 + 2\sigma$ , and we interpret the values estimated in these bins as arising from residual foregrounds and systematics. The remaining two  $k$ -bins are consistent with  $0 + 2\sigma$ . We have used the estimated  $\Delta^2(k)$  and  $\sigma$  values to place  $2\sigma$  upper limits  $\Delta_{UL}^2(k) = \Delta^2(k) + 2\sigma$  on the 21-cm brightness temperature fluctuations at different  $k$  bins (Table 3). We find the tightest constraint on the upper limits to be  $(133.97)^2$  mK $^2$  at the smallest bin  $k = 0.347$  Mpc $^{-1}$ . We have used the estimated  $\Delta_{UL}^2(k)$  to place corresponding  $2\sigma$  upper limits on  $[\Omega_{\text{H}_1} b_{\text{H}_1}]_{UL}$  (eq. 14). The values corresponding to the different  $k$ -bins are tabulated in Table 3. We obtain the tightest constraint of  $[\Omega_{\text{H}_1} b_{\text{H}_1}]_{UL} \leq 0.23$  from the smallest bin  $k = 0.347$  Mpc $^{-1}$ .

Ch21 have carried out a multi-redshift analysis of the same observational data after splitting it into several sub-bands of 8 MHz each. Their  $z = 2.19$  sub-band is closest to our analysis, and we have also shown their results in Figure 11 (orange line). We see that our present analysis extends to substantially smaller  $k$  values ( $0.347 < k < 7.584$  Mpc $^{-1}$ ) compared to Ch21 who have considered the  $k$ -range  $1 < k < 10$  Mpc $^{-1}$ . We find that in the common  $k$ -range  $1 < k < 8$  Mpc $^{-1}$  our  $\Delta^2(k)$  estimates are  $\sim 7$  times larger than those of Ch21. We also see that the  $2\sigma$  error bars on  $\Delta^2(k)$  are smaller in the present analysis as compared to Ch21 in the first five  $k$ -bins.

The difference can be attributed to the larger frequency bandwidth (24.4 MHz) used here. For the remaining three  $k$ -bins, the larger error bars may be attributed to lower sampling at longer baselines. Comparing the  $2\sigma$  upper limits, Ch21 have obtained  $(61.49)^2$  mK $^2$  and 0.11 respectively for  $\Delta^2(k)$  and  $[\Omega_{\text{H}_1} b_{\text{H}_1}]$  at  $k = 1$  Mpc $^{-1}$  whereas the present analysis reports  $(133.97)^2$  mK $^2$  and 0.23 respectively at  $k = 0.347$  Mpc $^{-1}$ .

We take this opportunity to highlight a key difference between the analysis method of Ch21 and the one used here. Considering the visibilities measured at the individual baselines, Ch21 have carried out a Fourier transform along frequency to estimate the visibilities in delay space (Morales & Hewitt 2004) which were then used (Parsons et al. 2012) to estimate the PS. The difficulty arises because the missing frequency channels (flagged due to RFI) introduce artefacts in the Fourier transform which corrupt the estimated PS. Ch21 have overcome this by using one dimensional complex CLEAN (Parsons & Backer 2009) to compensate for the missing frequency channels. In contrast, the method used here first correlates the visibility data across frequency channels to estimate  $C_\ell(\Delta\nu)$ . There are no missing frequency separations  $\Delta\nu$  in the estimated  $C_\ell(\Delta\nu)$  even though the visibility data has a substantial number of missing frequency channels. We have then used maximum likelihood to estimate the PS which is related to  $C_\ell(\Delta\nu)$  through a Fourier transform with respect to  $\Delta\nu$ . This method uses only the available frequency channels to estimate the PS, and it is not necessary to compensate for the missing frequency channels. For the present analysis we have validated this using simulations (Section 4) where the flagging of the simulated data exactly matches that of the actual data (55%). An earlier work (Bharadwaj et al. 2018) has used simulations to demonstrate that the present estimator is able to successfully recover the PS even when the data in 80% randomly chosen frequency channels are flagged.

## 6 SUMMARY AND CONCLUSIONS

H $_1$  21-cm intensity mapping is a promising tool to probe the large-scale structures in the Universe across a wide redshift range. In this paper we employ the TGE to estimate the MAPS  $C_\ell(\Delta\nu)$  and the PS  $P(k_\perp, k_\parallel)$  using data from four nights of uGMRT Band 3 observations of the ELAIS-N1 field. Our analysis is restricted to a 24.4 MHz sub-band which has a frequency resolution of 24.4 kHz and is centered at 432.8 MHz which corresponds to 21-cm signal from a redshift  $z = 2.28$ . Compact and discrete sources with flux densities  $> 100\mu\text{Jy}$  within an area of 1.8 deg $^2$  were identified and subtracted out. The residual visibility data was used for the analysis presented here. In addition to the individual nights data, we have also analysed the combined nights data.

The TGE (eq. 6) uses the measured visibilities to directly estimate  $C_\ell(\Delta\nu)$  which characterizes the second order statistics of the sky signal jointly as a function of the angular multipole  $\ell$  and frequency separation  $\Delta\nu$ . The TGE has three inherent advantages namely (1) it works with the gridded visibility data which makes it computationally fast; (2) it allows us to taper the sky response which reduces the foreground contamination from bright sources located in the side-lobes and the periphery of the telescope's field of view; (3) it uses the data to internally estimate the noise bias and subtracts this to provide an unbiased estimate of  $C_\ell(\Delta\nu)$ . We have used maximum likelihood (eq. 11) to determine  $P(k_\perp, k_\parallel)$  from the estimated  $C_\ell(\Delta\nu)$ , the two being related through a Fourier transform (eq. 9). We have validated the power-spectrum estimator using simulations (Section 4) which incorporate the flagging, frequency and baseline coverage of the actual data. As noted earlier, it is not necessary to compensate for

the missing frequency channels. Our analysis demonstrates that the estimator can recover the input model power spectrum with high accuracy over the entire  $k$  range used for the analysis presented in this paper (Figure 4).

The May 6 data has the least flagging and the minimum visibility r.m.s. (Table 2), and Figure 5 shows  $C_\ell(\Delta\nu)$  for different values of the tapering parameter  $f$  considering two values of  $\ell$ . Note that the tapering is more effective (sky response is narrower) as the value of  $f$  is reduced. Figure 6 shows  $C_\ell(\Delta\nu)$  for the full  $(\ell, \Delta\nu)$  range considered here. Considering  $f = 5$ , which may be loosely interpreted as no tapering, we find that  $C_\ell(\Delta\nu)$  exhibits oscillations in  $\Delta\nu$ , the frequency of the oscillations increases with  $\ell$ . We interpret these oscillations as arising from residual compact sources located at large angles from the phase center. We find that the overall amplitude as well as the amplitude of the oscillations in  $C_\ell(\Delta\nu)$  both decrease as  $f$  is varied from  $f = 5$  to  $f = 0.6$ . This demonstrates that the TGE is effective in tapering the sky response to suppress the contribution from sources in the outer region of the field of view. Both Figures 5 and 6 also show the results for the combined nights data with  $f = 0.6$ . Comparing this with May 6 with  $f = 0.6$ , we find that the oscillations and the overall amplitude of  $C_\ell(\Delta\nu)$  is even further reduced when we consider the combined nights data. This is a direct consequence of the higher baseline density (Figure 1) which makes the tapering more effective for the combined nights data in comparison to the May 6 data. This is due to the fact that tapering in the TGE is implemented through a convolution (eq. 3) which is more effective for the higher baseline density.

The different panels of Figure 7 shows  $|P(k_\perp, k_\parallel)|$  for four different cases. In all cases, the large values of  $|P(k_\perp, k_\parallel)|$  are mainly localized within the foreground wedge  $k_\parallel \leq [k_\parallel]_H$  (horizon), however we also find some foreground leakage beyond the predicted wedge boundary. Considering the May 6 data, we find that overall foreground amplitude and also the foreground leakage outside the wedge both come down as the value of  $f$  is reduced from  $f = 5$  to  $f = 0.6$ . There is an even further reduction when we consider the combined nights data with  $f = 0.6$ . We see that the combined nights data gives better results in comparison to the May 6 data, and we have used the combined nights data for the subsequent results and discussion here. Considering  $f = 5.0$  and  $f = 0.6$ , Figure 8 shows  $|P(k_\perp, k_\parallel)|$  as a function of  $k_\parallel$  for two different fixed  $k_\perp$  bins. We find the largest values of  $P(k_\perp, k_\parallel)$  ( $\sim 10^9 \text{ mK}^2 \text{ Mpc}^3$ ) at  $k_\parallel = 0$ . The value of  $|P(k_\perp, k_\parallel)|$  fall with increasing  $k_\parallel$ , and we find  $|P(k_\perp, k_\parallel)| \sim 10^4 - 10^5 \text{ mK}^2 \text{ Mpc}^3$  at the largest  $k_\parallel$  bins where the power oscillates between positive and negative values which are comparable with the  $1 - \sigma$  error-bars computed from system noise only simulations. We interpret the estimated power in this region as a combination of system noise and some residual foreground leakage. We also find that the values of  $|P(k_\perp, k_\parallel)|$  decrease when  $f$  is reduced from  $f = 5.0$  to  $f = 0.6$ .

An interesting feature seen in the various panels of Figure 7 and also in both the panels of Figure 8 is that the value of  $P(k_\perp, k_\parallel)$  does not decrease monotonically with increasing  $k_\parallel$ . Rather, it initially decreases and then increases again just beyond the horizon  $k_\parallel \approx [k_\parallel]_H$  after which it decreases again. This is more clearly visible at large  $k_\perp$ . We identify the rise in  $P(k_\perp, k_\parallel)$  close to the horizon limit as the pitchfork effect which has been reported earlier (Thyagarajan et al. 2015b; Kohn et al. 2016; Gehlot et al. 2018) in low frequency observations ( $\sim 150 \text{ MHz}$ ) which target the EoR 21-cm signal. The present work is possibly the first time that this effect is being reported at higher frequencies which target the post-reionization 21-cm signal.

The solid green curve in Figure 9 demarcates the region of  $(k_\perp, k_\parallel)$

space which we have identified to be relatively foreground-free and has been used to estimate the spherically binned power spectrum  $P(k)$ . We use the variable  $X$ , defined in eq. (17), to study the statistics of the estimated PS in this region (Figure 10). We find that for  $|X| \lesssim 20$  the P.D.F. is roughly symmetric with a positive mean  $\mu = 1.21$ . For  $|X| \lesssim 20$ , the P.D.F. is well described the t-distribution, beyond which ( $X > 20$ ) the t-distribution function underestimates the P.D.F. This indicates that the PS consists of some noise contributions as well as residual foregrounds. Modes within  $|X| \lesssim 20$  have a standard deviation  $\sigma_{Est} = 6.09$ , which suggests that the r.m.s. fluctuations estimated using the noise simulations underestimate the true errors by a factor  $\sigma_{Est} = 6.09$ . We rectify for this by considering the true errors as  $\delta P_N^{True}(k_\perp, k_\parallel) = \sigma_{Est} \times \delta P_N(k_\perp, k_\parallel)$ , which we carry forward for further analysis. Figure 11 shows the mean square brightness temperature fluctuations  $\Delta^2(k)$  along with  $2\sigma$  error bars considering 8 bins across the range  $0.347 \leq k \leq 7.584 \text{ Mpc}^{-1}$ . Table 3 lists these values along with  $\Delta_{UL}^2(k)$  the corresponding  $2\sigma$  upper limits. We find the tightest  $2\sigma$  upper limit of  $\Delta_{UL}^2(k) \leq (133.97)^2 \text{ mK}^2$  at  $k = 0.347 \text{ Mpc}^{-1}$  which translates to an upper limit  $[\Omega_{\text{H I}} b_{\text{H I}}]_{UL} \leq 0.23$ . Ch21 reported  $\Delta_{UL}^2(k) \leq (61.49)^2 \text{ mK}^2$  and  $[\Omega_{\text{H I}} b_{\text{H I}}]_{UL} \leq 0.11$  at  $k = 1 \text{ Mpc}^{-1}$ . The upper limits presented here are still orders of magnitude larger than the expected signal corresponding to  $\Omega_{\text{H I}} \sim 10^{-3}$  and  $b_{\text{H I}} \sim 2$ .

## ACKNOWLEDGEMENTS

We thank the scientific editor and the anonymous referee for their comments which have helped us in improving this work. We thank the staff of GMRT for making this observation possible. GMRT is run by National Centre for Radio Astrophysics of the Tata Institute of Fundamental Research. AG would like to acknowledge IUCAA, Pune for providing support through the associateship programme. SB would like to acknowledge funding provided under the MATRICS grant SERB/F/9805/2019-2020 of the Science & Engineering Research Board, a statutory body of Department of Science & Technology (DST), Government of India. Part of this work has used the Supercomputing facility ‘PARAM Shakti’ of IIT Kharagpur established under National Supercomputing Mission (NSM), Government of India and supported by Centre for Development of Advanced Computing (CDAC), Pune.

## DATA AVAILABILITY

The data from this study are available upon reasonable request to the corresponding author.

## REFERENCES

- Ali S. S., Bharadwaj S., 2014, *J. Astrophys. Astron.*, **35**, 157
- Anderson C. J., et al., 2018, *Monthly Notices of the Royal Astronomical Society*, **476**, 3382
- Bharadwaj S., Ali S. S., 2005, *MNRAS*, **356**, 1519
- Bharadwaj S., Pandey S. K., 2003, *J. Astrophys. Astron.*, **24**, 23
- Bharadwaj S., Sethi S. K., 2001, *J. Astrophys. Astron.*, **22**, 293
- Bharadwaj S., Srikant P. S., 2004, *J. Astrophys. Astron.*, **25**, 67
- Bharadwaj S., Nath B. B., Sethi S. K., 2001, *J. Astrophys. Astron.*, **22**, 21
- Bharadwaj S., Sethi S. K., Saini T. D., 2009, *Phys. Rev. D*, **79**, 083538
- Bharadwaj S., Pal S., Choudhuri S., Dutta P., 2018, *MNRAS*, **483**, 5694
- Bowman J. D., Morales M. F., Hewitt J. N., 2009, *ApJ*, **695**, 183



- Bull P., Camera S., Raccanelli A., Blake C., Ferreira P., Santos M., Schwarz D. J., 2015, in AASKA14. p. 24 ([arXiv:1501.04088](#))
- CHIME Collaboration et al., 2022, arXiv e-prints, p. [arXiv:2202.01242](#)
- Chakraborty A., et al., 2019a, *MNRAS*, 487, 4102
- Chakraborty A., et al., 2019b, *MNRAS*, 490, 243
- Chakraborty A., et al., 2021, *ApJ*, 907, L7
- Chang T.-C., Pen U.-L., Peterson J. B., McDonald P., 2008, *Phys. Rev. Lett.*, 100, 091303
- Chang T.-C., Pen U.-L., Bandura K., Peterson J. B., 2010, *Nature*, 466, 463
- Chen X., 2012, *International Journal of Modern Physics: Conference Series*, 12, 256
- Choudhuri S., Bharadwaj S., Ghosh A., Ali S. S., 2014, *MNRAS*, 445, 4351
- Choudhuri S., Bharadwaj S., Roy N., Ghosh A., Ali S. S., 2016a, *MNRAS*, 459, 151
- Choudhuri S., Bharadwaj S., Chatterjee S., Ali S. S., Roy N., Ghosh A., 2016b, *MNRAS*, 463, 4093
- Choudhuri S., Bharadwaj S., Ali S. S., Roy N., Intema H. T., Ghosh A., 2017, *MNRAS: Letters*, 470, L11
- Choudhuri S., Ghosh A., Roy N., Bharadwaj S., Intema H. T., Ali S. S., 2020, *MNRAS*, 494, 1936
- Datta K. K., Choudhuri T. R., Bharadwaj S., 2007, *MNRAS*, 378, 119
- Datta A., Bowman J. D., Carilli C. L., 2010, *ApJ*, 724, 526
- Eisenstein D. J., Hu W., 1998, *ApJ*, 496, 605
- Gehlot B. K., et al., 2018, *MNRAS*, 478, 1484
- Ghosh A., Bharadwaj S., Ali S. S., Chengalur J. N., 2011a, *MNRAS*, 411, 2426
- Ghosh A., Bharadwaj S., Ali S. S., Chengalur J. N., 2011b, *MNRAS*, 418, 2584
- Ghosh A., Prasad J., Bharadwaj S., Ali S. S., Chengalur J. N., 2012, *MNRAS*, 426, 3295
- Gupta Y., et al., 2017, *Current Science*, 113, 707
- Hazra D. K., Guha Sarkar T., 2012, *Phys. Rev. Lett.*, 109, 121301
- Kennedy F., Bull P., 2021, *MNRAS*, 506, 2638
- Kohn S. A., et al., 2016, *ApJ*, 823, 88
- Kumar J., Dutta P., Roy N., 2020, *MNRAS*, 495, 3683
- Kumar J., Dutta P., Choudhuri S., Roy N., 2022, *MNRAS*, 512, 186
- Masui K. W., et al., 2013, *ApJ*, 763, L20
- Mazumder A., Chakraborty A., Datta A., Choudhuri S., Roy N., Wadadekar Y., Ishwara-Chandra C. H., 2020, *MNRAS*, 495, 4071
- McMullin J. P., Waters B., Schiebel D., Young W., Golap K., 2007, in Shaw R. A., Hill F., Bell D. J., eds, *Astronomical Society of the Pacific Conference Series Vol. 376, Astronomical Data Analysis Software and Systems XVI*. p. 127
- Mondal R., Bharadwaj S., Iliev I. T., Datta K. K., Majumdar S., Shaw A. K., Sarkar A. K., 2019, *MNRAS*, 483, L109
- Morales M. F., Hewitt J., 2004, *ApJ*, 615, 7
- Morales M. F., Hazelton B., Sullivan I., Beardsley A., 2012, *ApJ*, 752, 137
- Murray S. G., Trott C. M., 2018, *ApJ*, 869, 25
- Newburgh L. B., et al., 2016, in Hall H. J., Gilmozzi R., Marshall H. K., eds, *Society of Photo-Optical Instrumentation Engineers (SPIE) Conference Series Vol. 9906, Ground-based and Airborne Telescopes VI*. p. 99065X ([arXiv:1607.02059](#)), doi:10.1117/12.2234286
- Noterdaeme P., et al., 2012, *A&A*, 547, L1
- Nuttall A. H., 1981, *IEEE Transactions on Acoustics Speech and Signal Processing*, 29, 84
- Offringa, A. R. van de Gronde, J. J. Roerdink, J. B. T. M. 2012, *A&A*, 539, A95
- Offringa A. R., de Bruyn A. G., Biehl M., Zaroubi S., Bernardi G., Pandey V. N., 2010, *MNRAS*, 405, 155
- Pal S., Bharadwaj S., Ghosh A., Choudhuri S., 2021, *MNRAS*, 501, 3378
- Parsons A. R., Backer D. C., 2009, *AJ*, 138, 219
- Parsons A. R., Pober J. C., Aguirre J. E., Carilli C. L., Jacobs D. C., Moore D. F., 2012, *ApJ*, 756, 165
- Pen U.-L., Staveley-Smith L., Peterson J. B., Chang T.-C., 2009, *MNRAS: Letters*, 394, L6
- Planck Collaboration et al., 2020, *A&A*, 641, A6
- Pober J. C., et al., 2016, *ApJ*, 819, 8
- Saha P., Bharadwaj S., Roy N., Choudhuri S., Chattopadhyay D., 2019, *MNRAS*, 489, 5866
- Saha P., Bharadwaj S., Chakravorty S., Roy N., Choudhuri S., Günther H. M., Smith R. K., 2021, *MNRAS*, 502, 5313
- Sarkar D., Bharadwaj S., Anathpindika S., 2016, *MNRAS*, 460, 4310
- Seo H.-J., Dodelson S., Marriner J., McGinnis D., Stebbins A., Stoughton C., Vallinotto A., 2010, *ApJ*, 721, 164
- Subrahmanya C. R., Manoharan P. K., Chengalur J. N., 2017, *J. Astrophys. Astron.*, 38, 10
- Swarup G., et al., 1971, *Nature Physical Science*, 230, 185
- Swarup G., Ananthkrishnan S., Kapahi V. K., Rao A. P., Subrahmanya C. R., Kulkarni V. K., 1991, *Current Science*, 60, 95
- Switzer E. R., et al., 2013, *MNRAS: Letters*, 434, L46
- Thyagarajan N., et al., 2015a, *ApJ*, 804, 14
- Thyagarajan N., et al., 2015b, *ApJ*, 807, L28
- Thyagarajan N., Parsons A. R., DeBoer D. R., Bowman J. D., Ewall-Wice A. M., Neben A. R., Patra N., 2016, *ApJ*, 825, 9
- Vedantham H., Udaya Shankar N., Subrahmanyan R., 2012, *ApJ*, 745, 176
- Visbal E., Loeb A., Wyithe S., 2009, *J. Cosmology Astropart. Phys.*, 2009, 030
- Wolz L., et al., 2021, *Monthly Notices of the Royal Astronomical Society*, 510, 3495
- Wuensche C., 2019, *Journal of Physics: Conference Series*, 1269, 012002
- Wyithe J. S. B., Loeb A., Geil P. M., 2008, *MNRAS*, 383, 1195
- Zafar T., Péroux C., Popping A., Milliard B., Deharveng J. M., Frank S., 2013, *A&A*, 556, A141

This paper has been typeset from a  $\text{\TeX}/\text{\LaTeX}$  file prepared by the author.